The Astrophysical Journal, 669:158–183, 2007 November 1

PROBING THE DARK MATTER AND GAS FRACTION IN RELAXED GALAXY GROUPS WITH X-RAY OBSERVATIONS FROM *CHANDRA* AND *XMM-NEWTON*

Fabio Gastaldello,[1] David A. Buote,[1] Philip J. Humphrey,[1] Luca Zappacosta,[1]
James S. Bullock,[1] Fabrizio Brighenti,[2,3] and William G. Mathews[2]

Received 2006 October 4; accepted 2007 June 18

ABSTRACT

We present radial mass profiles within $\sim 0.3 r_{\rm vir}$ for 16 relaxed galaxy groups—poor clusters (kT range 1–3 keV) selected for optimal mass constraints from the *Chandra* and *XMM-Newton* data archives. After accounting for the mass of hot gas, the resulting mass profiles are described well by a two-component model consisting of dark matter, represented by an NFW model, and stars from the central galaxy. The stellar component is required only for eight systems, for which reasonable stellar mass-to-light ratios (M/L_K) are obtained, assuming a Kroupa IMF. Modifying the NFW dark matter halo by adiabatic contraction does not improve the fit and yields systematically lower M/L_K. In contrast to previous results for massive clusters, we find that the NFW concentration parameter ($c_{\rm vir}$) for groups decreases with increasing $M_{\rm vir}$ and is inconsistent with no variation at the 3 σ level. The normalization and slope of the $c_{\rm vir}$-$M_{\rm vir}$ relation are consistent with the standard ΛCDM cosmological model with $\sigma_8 = 0.9$ (considering a 10% bias for early forming systems). The small intrinsic scatter measured about the $c_{\rm vir}$-$M_{\rm vir}$ relation implies that the groups represent preferentially relaxed, early forming systems. The mean gas fraction ($f = 0.05 \pm 0.01$) of the groups measured within an overdensity $\Delta = 2500$ is lower than for hot, massive clusters, but the fractional scatter ($\sigma_f/f = 0.2$) for groups is larger, implying a greater impact of feedback processes on groups, as expected.

Subject headings: cosmology: observations — dark matter — galaxies: halos — methods: data analysis — X-rays: galaxies: clusters

Online material: color figures

1. INTRODUCTION

The properties of dark matter (DM) halos are a powerful discriminator between different cosmological scenarios of structure formation. Dissipationless simulations of cold dark matter (CDM) models find that the radial density profiles of DM halos are fairly well described between approximately $0.01 r_{\rm vir}$ and $1 r_{\rm vir}$ (where $r_{\rm vir}$ is the virial radius) by the two-parameter Navarro-Frenk-White (NFW) model suggested by Navarro et al. (1997). Of particular importance is the distribution of halo concentration ($c_{\rm vir}$, the ratio between $r_{\rm vir}$ and the characteristic radius of the density profile, r_s) and $M_{\rm vir}$, the virial mass. Low-mass halos are more concentrated because they collapse earlier than halos of larger mass, thus producing a predicted correlation between $c_{\rm vir}$ and $M_{\rm vir}$. A significant scatter at fixed virial mass is expected and thought to be related to the distribution of halo formation epoch (e.g., Bullock et al. 2001; Wechsler et al. 2002). The $c_{\rm vir}$-$M_{\rm vir}$ relation and its scatter are a source of deviation from the self-similar scaling relation expected if the observable properties of halos are driven by simple gravitational collapse of the dominant DM component (e.g., Thomas et al. 2001). For the currently favored ΛCDM model the median $c_{\rm vir}$ varies slowly over a factor of 100 in $M_{\rm vir}$, whereas the scatter remains very nearly constant (e.g., Bullock et al. 2001; Dolag et al. 2004; Kuhlen et al. 2005). The precise relation between $c_{\rm vir}$ and $M_{\rm vir}$ is expected to vary significantly as a function of the cosmological parameters, including σ_8 and w, the dark energy equation of state (Dolag et al. 2004; Kuhlen et al. 2005), making an observational test of this relation a very powerful tool for cosmology.

High-quality X-ray data from *Chandra* and *XMM-Newton* observations indicate that the NFW model is a remarkably good description of the mass profiles of massive galaxy clusters out to large portions of their virial radii (e.g., Pratt & Arnaud 2002; Lewis et al. 2003; Pointecouteau et al. 2005; Vikhlinin et al. 2006; Zappacosta et al. 2006). Typical values and scatter of concentrations determined from the samples of clusters analyzed in Pointecouteau et al. (2005) and Vikhlinin et al. (2006) are in general agreement with the simulation results. The $c_{\rm vir}$-$M_{\rm vir}$ relation measured by Pointecouteau et al. (2005), when fitted with a power law, has a slope of $\alpha = -0.04 \pm 0.03$. This slope is quite consistent with a constant value and is marginally consistent ($\approx 2\,\sigma$) with ΛCDM (Dolag et al. 2004). The optical study by Łokas et al. (2006) using galaxy kinematics for six nearby relaxed Abell clusters obtained results consistent with the above X-ray studies but with larger uncertainty (e.g., $\alpha = -0.6 \pm 1.3$).

Observational tests of ΛCDM have proven controversial at the galaxy scale (see discussion in Humphrey et al. 2006). Recently, using high-quality X-ray *Chandra* data, in Humphrey et al. (2006) we obtained accurate mass profiles for seven elliptical galaxies, well described by a two-component model comprising an NFW DM halo and a stellar mass component. Omitting the latter component, which dominates the mass budget in the inner regions, leads to unphysically large concentrations (see also Mamon & Łokas 2005) and may explain some large values found in the literature for elliptical galaxies (Sato et al. 2000; Khosroshahi et al. 2004). The measured $c_{\rm vir}$-$M_{\rm vir}$ relation of the seven galaxies generally agrees with ΛCDM, provided that the galaxies represent preferentially relaxed, earlier forming systems.

Very few constraints exist on the group scale, where the simulations of DM halos are more reliable, compared to massive clusters, because a large number of objects can be simulated at once (e.g., Bullock et al. 2001). Sato et al. (2000) investigated the c-M relation in X-rays using *ASCA* for a sample of objects ranging

[1] Department of Physics and Astronomy, University of California at Irvine, Irvine, CA 92697-4575.
[2] University of California Observatories/Lick Observatory, University of California, Santa Cruz, CA 95064.
[3] Dipartimento di Astronomia, Università di Bologna, Bologna 40127, Italy.

from 10^{12} to 10^{15} $M_{\odot}$, including objects in the mass range discussed in this paper. (However, neither the names of the objects in their sample nor the description of the data reduction and analysis have appeared in the literature.) The slope obtained for the *c*-*M* relation was steep, -0.44 ± 0.13. The limited spatial resolution of *ASCA* and energy dependence of its point-spread function (PSF) made problematic the determination of reliable density and temperature profiles, and the authors neglected any stellar mass component in their fits. Optical studies of groups using galaxy-galaxy lensing (Mandelbaum et al. 2006) and caustics in redshift space (Rines & Diaferio 2006) obtain $c_{\rm vir}$-$M_{\rm vir}$ relations that are consistent with CDM simulations and with no variation in c with M, but with large errors.

The scale of galaxy groups is also particularly interesting for the investigation of the influence of baryons on the DM profile. While the stellar mass component is clearly distinguished from the NFW DM component in the gravitating mass profiles obtained from *Chandra* observations of elliptical galaxies (Humphrey et al. 2006), X-ray studies of relaxed clusters do not report significant deviations from a single NFW profile fitted to the gravitating mass (Lewis et al. 2003; Pointecouteau et al. 2005; Vikhlinin et al. 2006; Zappacosta et al. 2006), except for a few group-scale objects (Vikhlinin et al. 2006). The group scale seems to represent a transition in the character of the mass profiles (and temperature profiles; Humphrey et al. 2006) and needs to be systematically explored.

X-ray studies of mass profiles in galaxy systems have the advantage that the pressure tensor of the hot gas is isotropic and the gas in hydrostatic equilibrium (HE) traces the entire three-dimensional (3D) cluster potential well. If one is careful to choose relaxed objects (i.e., with smooth, regular X-ray images), then hydrostatic equilibrium is a good approximation and the resulting gravitating mass is reliable, accurate to at least $\sim$15% even in the presence of turbulence (e.g., Evrard et al. 1996; Faltenbacher et al. 2005; Nagai et al. 2007). Because of limitations of previous X-ray telescopes like *Röntgensatellit* (*ROSAT*) and *ASCA*, some simplifying assumptions like isothermality had to be made for the determination of group masses (see Mulchaey 2000 and references therein). *Chandra* and *XMM-Newton* have provided for the first time high-quality, spatially resolved spectra of the diffuse hot gas of X-ray groups (e.g., Buote et al. 2003, 2004; Sun et al. 2003; O'Sullivan et al. 2003; Pratt & Arnaud 2005).

An investigation of the detailed mass profiles of galaxy groups ($M = 10^{13}$–10^{14} $M_{\odot}$) with higher quality *Chandra* and *XMM-Newton* data is, therefore, timely. In this paper we present measurements of the mass profiles of a sample of 16 groups chosen to provide the best mass determinations with current X-ray data. We selected the objects both to be the most relaxed systems (i.e., very regular X-ray image morphology), to ensure that hydrostatic equilibrium is a good approximation, and to have the highest quality *Chandra* and *XMM-Newton* data, which allow for the most precise measurements of the gas density and temperature profiles. This paper is part of a series (see also Humphrey et al. 2006; Zappacosta et al. 2006; Buote et al. 2007) using high-quality *Chandra* and *XMM-Newton* data to investigate the mass profiles of galaxies, groups, and clusters, placing constraints on the $c_{\rm vir}$-$M_{\rm vir}$ relation over $\approx$2.5 orders of magnitude in $M_{\rm vir}$. It is also the first in a series investigating the X-ray properties of groups and poor clusters: in future papers we will investigate the entropy and heavy-element abundance profiles. This paper is organized as follows. We discuss the target selection in § 2 and the data reduction in § 3. We discuss the spectral analysis in § 5, the mass analysis in § 6, and present the results in § 7. We discuss the results for individual objects in the sample in § 8, comparing with previous work in the literature. The systematic uncertainties in our analysis are discussed in § 9, and we present a discussion of our results in § 10, with our conclusions in § 11. All distance-dependent quantities have been computed assuming $H_0 = 70$ km s^{-1} Mpc^{-1}, $\Omega_m = 0.3$, and $\Omega_{\Lambda} = 0.7$. Our assumed virial radius is defined as the radius of a sphere of mass $M_{\rm vir}$, the mean density of which (for redshift 0) is 101 times the critical density of the universe (appropriate for the assumed cosmological model) and estimated at the redshift of the object. We quote values for concentrations and masses at different overdensities to ease comparison with previous work in Appendix A. Our analysis procedure is described in greater detail in Appendix B. All the errors quoted are at the 68% confidence limit.

2. TARGET SELECTION

For this study we choose, whenever possible, to focus on X-ray–bright objects observed by both *Chandra* and *XMM-Newton* to exploit the complementary characteristics of the two satellites. The unprecedented spatial resolution of *Chandra* allows the temperature and density profiles to be resolved in the core, allowing us to disentangle the stellar and DM components. The unprecedented sensitivity of *XMM-Newton* ensures good signal-to-noise ratio (S/N) even in the faint outer regions, which is crucial because good constraints on the virial mass of the halo require density and temperature constraints over as large a radial range as possible. We looked for bright objects in the temperature range 1–3 keV with sufficiently long exposures in the *Chandra* and *XMM-Newton* archives, together with our proprietary data. The potential targets were processed (§ 3) and the images in the 0.5–10 keV band examined (§ 4) for evidence of disturbances: we choose objects that have a very regular X-ray morphology, showing no or only weak signs of dynamical activity, with the peak of the emission coincident with a luminous elliptical galaxy that is the most luminous group member. The only exception is RGH 80, which has two elliptical galaxies of comparable sizes in the core and probably a submerging group in the south (Mahdavi et al. 2005). We include this object because it is part of a complete, X-ray flux-limited sample of 15 groups that is scheduled to be observed by *Chandra*. It also allows an interesting comparison of derived mass properties with those obtained for the obviously relaxed systems in the sample.

The details of the observations are given in Table 1. We do not consider for analysis the available *XMM-Newton* observations of ESO 3060170, MS 0116.3−0115, and RX J1159.8+5531 because they are heavily contaminated by flares. We also do not consider the *Chandra* observation of ESO 5520200 because of insufficient S/N for our purposes. In order to use as large a radial range as possible for objects observed in the ACIS-S configuration but lacking *XMM-Newton* data (MS 0116.3−0115 and RX J1159.8+5531), we follow Vikhlinin et al. (2006) and also use the ACIS-S2 CCD in the analysis.

The present sample has been selected preferentially for X-ray brightest and most relaxed groups to obtain the best constraints on the mass profiles in individual objects with current data. Although the sample is biased and is not statically complete, our analysis of these systems represents an essential step in the investigation of DM in galaxy groups with X-rays. In future work we will compare these results to those obtained using the complete, X-ray flux-limited sample of 15 groups noted above.

3. DATA REDUCTION

3.1. *Chandra*

For data reduction we used the CIAO 3.2 and HEAsoft 5.3 software suites, in conjunction with the *Chandra* CALDB calibration

TABLE 1
THE GROUP SAMPLE AND JOURNAL OF OBSERVATIONS

Group	z	Distance (Mpc)	ACIS Aim Point	*Chandra* Exposure (ks)	EPIC Filter	pn Mode	*XMM-Newton* Exposure (ks)	r_{out}[a] (kpc)	Δ[b]
NGC 5044	0.0090	38.8	S	20.2	Thin	FF	19.5/19.3/8.9 + 38.4/38.4/32.0[c]	326	101.9
NGC 1550	0.0124	53.6	I	9.8 + 9.6[d]	Medium	FF	21.4/22.6/17.8	213	102.2
NGC 2563	0.0149	64.5	...	...	Medium	FF	20.4/20.8/16.5	219	102.4
A262	0.0163	70.7	S	28.7	Thin	EFF	23.5/23.4/15.0	254	102.5
NGC 533	0.0185	80.3	S	36.7	Thin	FF	38.1/37.4/30.1	271	102.7
MKW 4	0.0200	87.0	S	29.8	Medium	EFF	14.0/13.9/9.4	336	103.1
IC 1860	0.0223	97.1	...	...	Thin	FF	34.1/34.8/28.0	323	103.1
NGC 5129	0.0230	100.2	...	...	Medium	FF	10.9/12.0/10.7	241	103.1
NGC 4325	0.0257	112.2	S	30.0	Thin	FF	20.8/20.8/14.7	238	103.3
ESO 5520200	0.0314	137.7	...	...	Thin	EFF	32.2/32.2/26.7	418	103.8
AWM 4	0.0317	139.0	...	...	Medium	EFF	17.5/17.2/12.5	455	103.9
ESO 3060170	0.0358	157.5	I	13.8 + 13.9[d]	...	...	...	245	104.2
RGH 80	0.0379	167.0	S	38.5	Thin	EFF	32.8/32.6/26.3	533	104.4
MS 0116.3−0115	0.0452	200.2	S	39.0	...	...	...	350	105.0
A2717	0.049	217.7	...	...	Thin	FF	49.2/49.6/42.9	730	105.3
RX J1159.8+5531	0.081	368.0	S	75.0	...	...	...	625	108.0

NOTES.—Listed in the table are the groups in our sample. Redshifts were obtained from NED, and the distance is the inferred luminosity distance for a cosmological model with $H_0 = 70$ km s^{-1} Mpc^{-1}, $\Omega_m = 0.3$, and $\Omega_\Lambda = 0.7$. The ACIS aim point refers to S if the aim point is located on the S3 chip or to I if the aim point is located on one of the ACIS-I chips. The ACIS mode of all the observations was the Very Faint mode. The pn mode refers to FF if it is full frame or to EFF if it is extended full frame; the MOS detectors were always in FF mode. The exposure times are net exposure times, after flare cleaning as described in the text, and for *XMM-Newton* they refer to MOS1/MOS2/pn.

[a] The outer radius used in our analysis.

[b] The assumed overdensity, calculated at the redshift of the object.

[c] The first set of exposures refers to the central pointing and the second set to the offset pointing.

[d] Observed twice with ACIS-I, with the core centered on ACIS-I0 in one occasion and on ACIS-I1 in the other.

database 3.0.0. In order to ensure the most up-to-date calibration, all data were reprocessed from the "level 1" event files, following the standard *Chandra* data reduction threads.[4] We applied corrections to take account of a time-dependent drift in the detector gain and, for ACIS-I observations, the effects of "charge transfer inefficiency," as implemented in the standard CIAO tools. From regions of least source contamination of the CCDs we extracted a light curve (5.0–10.0 keV) to identify periods of high background. Point-source detection was performed using the CIAO tool `wavdetect` (Freeman et al. 2002). The source lists created in different energy bands (so as to identify unusual soft or hard sources) were combined, and duplicated sources were removed. The final list was checked by visual inspection of the images. The resolved point sources were finally removed so as not to contaminate the diffuse emission. Further details about the *Chandra* data reduction can be found in Humphrey & Buote (2006).

3.2. *XMM-Newton*

We generated calibrated event files with SAS version 6.0.0 using the tasks `emchain` and `epchain`. We considered only event patterns 0–12 for MOS and 0 for pn. Bright pixels and hot columns were removed by applying the expression (FLAG = 0) to the extraction of spectra and images. We correct statistically for the pn out-of-time (OoT) events. Following the standard procedure, we generate an OoT event list, processed in the same way as the observation, and then subtract it from the images and spectra, after being multiplied by the mode-dependent ratio of integration and readout time (6.3% for full frame and 2.3% for extended full frame). The energy scale of the pn over the whole spectral bandpass has been further improved using the task `epreject`. We clean the data for soft proton flares using a threshold cut method by means of a Gaussian fit to the peak of the histogram of the 100 s time bins of the light curve (see Appendix A of Pratt & Arnaud 2002; De Luca & Molendi 2004) and excluding periods where the count rate lies more than 3 σ away from the mean. The light curves were extracted from regions of least source contamination (excising the bright group core in the central 5′ and the point-source list from the SOC pipeline, after visual inspection) in two different energy bands: a hard band, 10–12 keV for MOS and 10–13 keV for pn, and a wider band, 0.5–10 keV, as a safety check for possible flares with soft spectra (Nevalainen et al. 2005; Pradas & Kerp 2005). The flaring periods thus determined were further checked by visual inspection of the light curves. Point sources were detected using the task `ewavelet` in the energy band 0.5–10 keV and checked by eye on images generated for each detector. Detected point sources from all detectors were merged, and the events in the corresponding regions were removed from the event list, using circular regions of 25″ radius centered at the source position. The area lost due to point-source exclusion, CCD gaps, and bad pixels was calculated using a mask image. Redistribution matrix files (RMFs) and ancillary response files (ARFs) were generated using the SAS tasks `rmfgen` and `arfgen`, the latter in extended source mode. Appropriate flux weighting was performed for RMFs, using our own dedicated software, and for ARFs, using exposure-corrected images of the source as detector maps (with pixel size of 1′, the minimum scale modeled by `arfgen`) to sample the variation in emission, following the prescription of Saxton & Siddiqui (2002). Spectral results obtained using ARFs are completely consistent with the other frequently employed method (e.g., Arnaud et al. 2001) of correcting directly the spectra for vignetting (Gastaldello et al. 2003; Morris & Fabian 2005).

3.3. *Background Subtraction*

Ensuring proper background subtraction is one of the key challenges associated with the spectral fitting of low surface brightness, diffuse X-ray emission. The background experienced by both

[4] See http://cxc.harvard.edu/ciao/threads/index.html.

Chandra and *XMM-Newton* consists of (1) an extreme time-variable component due to soft ($E \sim$ tens of keV) protons channeled by the telescopes mirrors, (2) a slowly changing (with variability timescale much longer than the length of a typical observation) quiescent component due to high-energy particles ($E >$ few MeV), and (3) the sky X-ray background, decomposed into the extragalactic cosmic X-ray background by active galactic nuclei (AGNs) and the Galactic X-ray emission (e.g., Lumb et al. 2002; Markevitch et al. 2003).

The "blank fields" distributed by the observatories are not a perfect representation of the background in any one observation. First, there are significant long-term variations in the quiescent particle background. Second, the soft Galactic background component varies strongly from field to field. Finally, there may be some residual mild flaring.

Two approaches have been investigated to obtain more accurate background estimates than provided by the blank-field background templates: the double subtraction technique (see details in Appendix A of Arnaud et al. 2002) and a complete modeling of the various background components (e.g., Lumb et al. 2002; Markevitch et al. 2003). Double subtraction is, in principle, very effective, but particular care has to be taken to locate a region in the field of view of the observation completely free of source emission; this is difficult for nearby objects. The complete modeling of the various background components can rely on a large number of observations performed to characterize the quiescent particle background component (stowed or dark Moon for *Chandra*, *closed* for *XMM-Newton*) and on the large number of observations that constitute the blank-field data sets to characterize the sky background components. The drawback is that the resulting model, which also includes a source component, is complicated, and parameter degeneracies can arise. However, the method is particularly effective for studying groups and poor clusters because the source component (mainly characterized by the $\sim$1 keV Fe L-shell blend) is clearly spectrally separated from all the other background components. For the use of this approach to the *Chandra* data we refer the reader to Humphrey & Buote (2006). Here we describe the procedure used for *XMM-Newton* data that elaborates and updates the procedure described in Buote et al. (2004). The algorithm implemented has the following main steps:

1. Characterization of the quiescent particle background. We co-add individual spectra taken from *closed* observations. The spectra in the 0.4–12 keV band for MOS and the 0.4–13 keV band for pn can be adequately described by a broken power-law continuum and several Gaussians for the instrumental lines. Typical values for the model parameters are 0.7–0.8 for the slope at low energies, 1.0–1.2 keV for the break energies, 0.2 for the high-energy slope for MOS, and 0.4–0.5 for the high-energy slope for pn. While the low-energy slope exhibits significant variation between the observations in our study, the high-energy slope is very stable. These results are consistent with previous studies (Lumb et al. 2002; De Luca & Molendi 2004; Nevalainen et al. 2005). The spectral shape of the continuum broken power law does not change significantly across the detector, nor does it vary in time (as in the MOS study by De Luca & Molendi 2004) at high energies.

2. The model derived from the *closed* data is fitted to the spectra of the out-of-field-of-view (OFV) events of each observation. Portions of the MOS and pn detectors are not exposed to the sky, and therefore neither cosmic X-ray photons nor low-energy particle–induced events (like from soft protons) are collected. Indeed, while this is almost exactly true for the MOS (the fraction of OoT events is 0.35% in FF mode), for the pn a higher fraction of in-FOV events are assigned to the OFV region as OoT (6.3% in FF mode and 2.3% in EFF). In the case of strong flaring, this OoT contribution can seriously affect the pn OFV spectrum. We therefore chose to extract OFV events for the pn after the flare cleaning. The model derived from the OFV data is taken as the initial representation of the quiescent particle background for the particular observation.

3. To the broken power-law plus Gaussian lines describing the quiescent instrumental background (not vignetted and implemented as a background model in XSPEC), we add the components describing the sky X-ray background, following Lumb et al. (2002): a power law with slope $\Gamma = 1.41$ and normalization, as reported in De Luca & Molendi (2004), free to vary within the cosmic variance as $\Omega^{-1/2}$ (Barcons et al. 2000), where Ω is the solid angle covered by the observation; and two thermal components with temperatures 0.07 and 0.20 keV, respectively, and abundances fixed at solar. When modeling sources projected toward the North Polar Spur (NGC 5129), we found it necessary to add a third thermal component at $\sim$0.4 keV, in agreement with Markevitch et al. (2003) and Vikhlinin et al. (2005).

4. This model, plus a source component described by a thermal plasma with temperature and abundance free to vary, was fitted jointly to the outermost annuli used in the spectral extraction (see below). The parameters of the source component were free to vary in each annulus. The normalizations of the cosmic components and of the broken power-law component were scaled according to the ratio of the annuli area, while the normalizations of the instrumental lines were free to vary, given the fact that these components are highly spatially variable (e.g., De Luca & Molendi 2004; Lumb et al. 2002). An intercalibration constant free to vary between 0.9 and 1.1 was added to the model to take into account any cross calibration differences between the three EPIC instruments. Given the best-fit model for these annuli, we generate a pulse-height amplitude (PHA) correction file used in XSPEC.

5. For the annuli not involved in the background fitting, we scale the resulting model to the area of the annular region of interest in the spectral extraction and generate a PHA file. To take into account the variable instrumental lines, we renormalized the instrumental line components in the model using the corresponding regions extracted from the background templates.

We mention that possible slight variations in the particle continuum across the detector plane (see Appendix A of De Luca & Molendi 2004), or residual mild flaring, have been modeled by slightly changing the high-energy slope of the broken power law. This does not have any tangible effect on the spectral parameters derived for soft X-ray sources like the objects considered in this paper.

4. X-RAY IMAGES

The X-ray image of each group was examined to identify any significant surface brightness disturbances indicating departures from hydrostatic equilibrium. Low-level X-ray disturbances like the weak signs of AGN activity in the center of Abell 262 (Blanton et al. 2004), or the presence of a submerging group in the south of RGH 80 (Mahdavi et al. 2005), do not seriously impact X-ray mass determinations, provided that care is taken to avoid highly disturbed emission (Buote & Tsai 1995; Schindler 1996). The images for 15 objects in the sample are shown in Figure 1: for objects that have *XMM-Newton* data we show the combined MOS1 and MOS2 image in the 0.5–2.0 keV band. For those objects with only *Chandra* data (3 out of 16) we did the following: For RX J1159.8+5531 and MS 0116.3−0115 we display the 0.5–10 keV ACIS-S3 image, while for ESO 3060170 we show the 0.5–10 keV

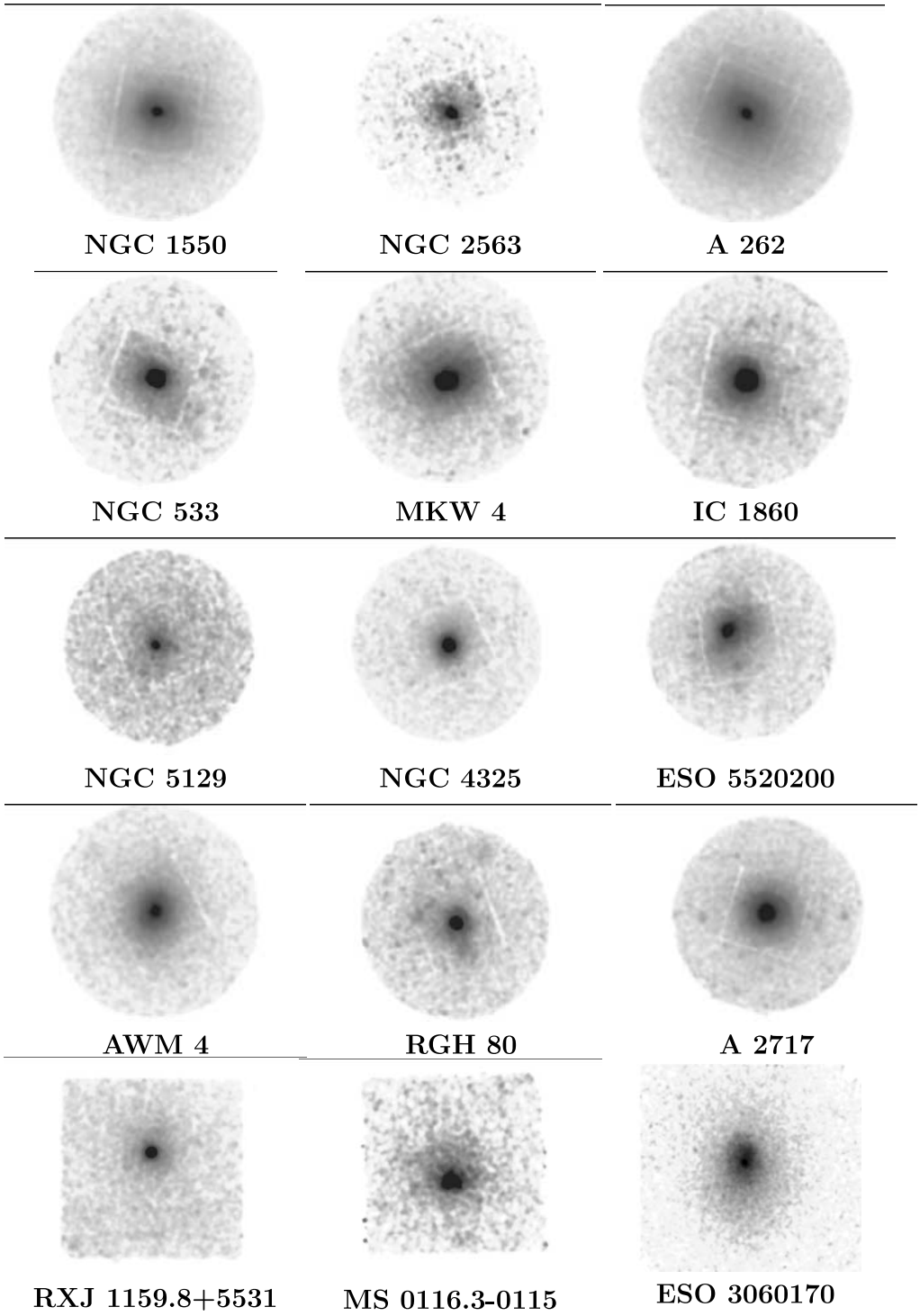

FIG. 1.—X-ray images of each of the objects in the sample (see § 4). [*See the electronic edition of the Journal for a color version of this figure.*]

ACIS-I image. The images were processed to remove point sources using the CIAO tool `dmfilth`, which replaces photons in the vicinity of each point source with a locally estimated background. The images were then flat-fielded with a 1.7 keV exposure map for *Chandra* images and a 1.25 keV exposure map for *XMM-Newton*. Then we smoothed the images with a 5″ Gaussian for *Chandra* and a 16″ Gaussian for *XMM-Newton* to make large-scale structure more apparent. For both the *Chandra* and *XMM-Newton* images of NGC 5044 we refer the reader to Buote et al. (2003).

None of the objects show obvious large-scale disturbance in their X-ray emission. The only notable substructure is the infalling subgroup in the southern region of RGH 80, evident as a tail of enhanced emission. Some disturbance is also present in the core of RGH 80 as revealed by our *Chandra* image. We masked in our analysis the region of enhanced X-ray emission associated with the subgroup. For other systems some low-amplitude, small-scale disturbances are present, such as a surface brightness discontinuity, reminiscent of a cold front, in the northwest of IC 1860; the cavities in the central 10 kpc of Abell 262, as revealed by the *Chandra* image presented in Blanton et al. (2004); and the filamentary structures and possible cavities in NGC 5044 (Buote et al. 2003). The "cooling wake" discussed in the *XMM-Newton* image

of NGC 5044 by Finoguenov et al. (2006) is simply the bright southeast arm of the finger-like structure caused by the cavities. Hints of cavities have been detected in NGC 4325 (Russell et al. 2007), and there are signs of sloshing in the core of MKW 4. We assess the impact of these features in § 9.6.

5. SPECTRAL ANALYSIS

We extracted spectra in concentric circular annuli located at the X-ray centroid computed within a radius of 30″, with the initial center on the peak of the X-ray emission. The widths of the annuli were chosen to have approximately equal background-subtracted counts and to have a minimum width of 60″ for *XMM-Newton* to avoid undersampling of the PSF. For *Chandra*, given the better PSF, the widths of the annuli, in practice, were only limited by count statistics. The spectra were rebinned to ensure an S/N of at least 3 and a minimum 20 counts bin^{-1} (necessary for the validity of the χ^2 minimization method). We fitted the background-subtracted spectrum with an APEC thermal plasma modified by Galactic absorption (Dickey & Lockman 1990) to each annulus. The free parameters are temperature, normalization (proportional to emission measure), and the abundances Fe, O, and, when possible, Si and S. The impact of unresolved point sources, in particular low-mass X-ray binaries (LMXBs) in the central galaxy, was taken into account by adding a 7.3 keV bremsstrahlung component for all annuli within the 25th magnitude isophote (D_{25}) of the central galaxy, taken from Leda (this model gives a good fit to the composite spectrum of the detected sources in nearby galaxies; Irwin et al. 2003). This is particularly relevant for the inner *XMM-Newton* annuli, where in general point sources are not detected. The spectral fitting was performed with XSPEC (ver. 11.3.1; Arnaud 1996). We estimated the statistical errors on the fitted parameters by simulating spectra for each annulus using the best-fitting models and then fitted the simulated spectra in exactly the same manner as done for the actual data. From 20 Monte Carlo simulations we compute the standard deviation for each free parameter, which we quote as the "1 σ" error (these error estimates generally agree very well with those obtained using the standard $\Delta\chi^2$ approach in XSPEC; e.g., Humphrey & Buote 2006).

If an object has been observed by both *Chandra* and *XMM-Newton*, we selected for our final analysis only the *Chandra* data in the inner core region where the temperature rises outward from the center. The *XMM-Newton* spectra extracted in wide annuli are not as well fitted by a single-temperature emission model as are the *Chandra* spectra in narrower annuli, suggesting that departures from single-temperature emission in the projected spectra stem primarily from the steep radial temperature gradient present in the core, as shown in Figure 2 for NGC 533. The better *Chandra* PSF also allows us to exclude point sources undetected with *XMM-Newton*, in particular LMXBs in the central galaxy. Unresolved LMXBs still affect the *Chandra* data, but to a much lesser extent than *XMM-Newton* data. This component is evident as an excess at energies greater than ~3 keV and can contribute, if neglected, to the multiphase appearance of *XMM-Newton* spectra.

6. MASS MODELING

To calculate the gravitating mass distribution, we solve the equation of hydrostatic equilibrium assuming spherical symmetry. By requiring spherical symmetry, we obtain spherically averaged mass profiles, which allows us to test the spherically averaged DM profiles obtained from cosmological simulations and to facilitate comparison to previous observational studies.

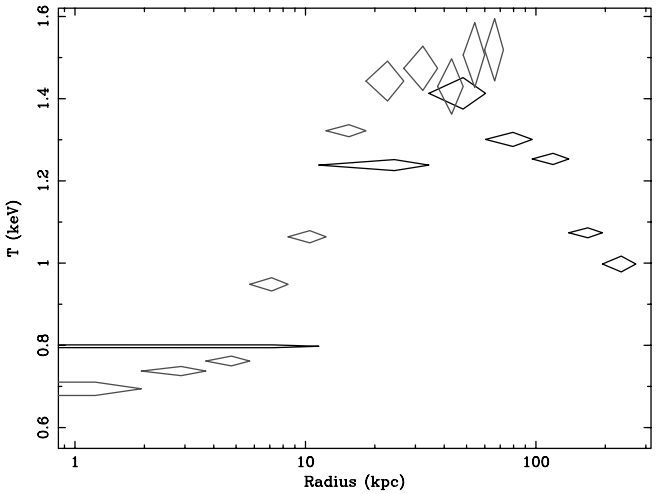

FIG. 2.—Temperature profile for the NGC 533 group derived from *XMM-Newton* data (*black*) and from *Chandra* data (*gray*). The inner two *XMM-Newton* bins have not been considered in the derivation of the mass profile. [*See the electronic edition of the Journal for a color version of this figure.*]

Following the approach adopted in Humphrey et al. (2006), we assume parameterizations for the temperature and mass profiles to calculate the gas density assuming hydrostatic equilibrium,

$$\rho_g(r) = \rho_{g0}\frac{T_0}{T(r)}\exp\left(\frac{-\mu m_A G}{k_{\rm B}}\int_{r_0}^{r}\frac{M\,dr}{r^2 T}\right), \qquad (1)$$

where r is the radius from the center of the gravitational potential, ρ_g is the gas density, ρ_{g0} and T_0 are density and temperature at some "reference" radius r_0, $k_{\rm B}$ is Boltzmann's constant, G is the universal gravitational constant, m_A is the atomic mass unit, and μ (taken to be 0.62) is the mean atomic weight of the gas. The $\rho_g(r)$ and $T(r)$ profiles are fitted simultaneously to the data to constrain the parameters of the temperature and mass models. Since the gravitating mass also contains the gas mass, equation (1) is solved iteratively for ρ_g.

This "parametric mass method" is the principal approach employed in this study. We assess systematic errors in this adopted method in § 9.5 by comparing to results obtained using other solutions to the hydrostatic equilibrium equation. First, rather than solving for the gas density, we can solve for the temperature,

$$T(r) = T_0\frac{\rho_{g0}}{\rho_g(r)} - \frac{\mu m_A G}{k_{\rm B}\rho_g(r)}\int_{r_0}^{r}\frac{\rho_g M\,dr}{r^2}, \qquad (2)$$

which provides an alternative implementation of the parametric mass method. Note that in both cases the parameters of the mass model are obtained from fitting the gas density and temperature data. The goodness of fit for any mass model (e.g., NFW) can be assessed directly from the residuals of the fit. Second, we use the more traditional formulation of the hydrostatic equilibrium equation (Mathews 1978),

$$M(<r) = r\frac{k_{\rm B}T(r)}{G\mu m_A}\left(-\frac{d\ln\rho_g}{d\ln r} - \frac{d\ln T}{d\ln r}\right), \qquad (3)$$

which involves parameterizing independently ρ_g and T using simple functional forms in order to evaluate the derivatives in equation (3). Since, however, the mass profile itself is not parameterized, we denote this traditional approach a "nonparametric mass method." Since the mass profile itself is produced by this method, if one

wants to evaluate the success of a particular mass model (e.g., NFW), then additional fitting is required. Consequently, following previous studies (e.g., Lewis et al. 2003), for each annulus we assign a 3D radius value $r \equiv [(R_{\rm out}^{3/2} + R_{\rm in}^{3/2})/2]^{2/3}$, where $R_{\rm in}$ and $R_{\rm out}$ are, respectively, the inner and outer radii of the (two-dimensional [2D]) annulus. At each radius r we calculate the total enclosed gravitating mass $M(<r)$ according to the equation of hydrostatic equilibrium. The errors on the resulting mass "data points" were estimated from the Monte Carlo simulations used to estimate the errors for density and temperatures (§ 5), giving a set of mass values at each radius. From those we calculate the standard deviation, which we quote as the "1 σ" error for this method. To analyze the shape of the mass profiles, we fitted parameterized models to the mass values.

There are several reasons why we adopt equation (1) instead of equation (3) for our analysis. First, as noted above, the parametric mass method allows a particular mass model to be constrained immediately by the gas density and temperature data and the goodness of fit of the mass model can be assessed in a straightforward manner. Second, despite the high-quality X-ray data provided by *Chandra* and *XMM-Newton*, it is still not possible to compute accurate derivatives of the temperature and density profiles at each radius. Consequently, smooth models must be fitted to the entire radial profiles, which may not produce physical solutions to equation (3), e.g., jagged, nonmonotonically increasing mass profiles. Third, we analyze the projected temperatures and densities, which requires the models for the gas density (density squared; see below) and temperature to be projected along the line of sight. This requires evaluating the models at least out to the virial radius, well outside the outer radius of most of the groups in our sample. By using the parametric mass method, any extrapolation of the gas density (eq. [1]) or temperature (eq. [2]) is performed consistently within the context of the assumed mass profile. It is for this last reason that we have a slight preference for using equation (1) over equation (2) for this study. Nevertheless, despite these differences, we find that the different approaches to the mass modeling represented by the three equations give consistent results, within the errors, for the global halo properties (see also § 9.5).

For our default analysis we projected parameterized models of the 3D quantities, ρ_g^2 and T, and fitted these projected models to the results obtained from our analysis of the data projected on the sky (see § 5). The models have been integrated over each radial bin (rather than only evaluating at a single point within the bin) to provide a consistent comparison. They also have been projected along the line of sight, including the radial variation in the plasma emissivity $\Lambda(T, Z_{\rm Fe})$, using a model fitted to the observed $Z_{\rm Fe}$ profile. We provide a review of the projection of spherical coronal gas models for comparison to X-ray spectral data in Appendix B.

In the left panels of Figures 3, 4, 5, and 6 we show the radial profiles of the emission-weighted projection of ρ_g^2 (i.e., proportional to the norm parameter of the APEC model divided by the area of the annulus) along with the best-fitting model and residuals; in the middle panels we show the radial profiles of the measured T along with the best-fitting emission-weighted projected model and residuals.

6.1. *Gas Density Models*

We considered two models for fitting of the gas density profile: the β model (Cavaliere & Fusco-Femiano 1978) and a cusped β model (Pratt & Arnaud 2002; Lewis et al. 2003), the latter of which is a modified β model allowing for steepening of the profile in the inner regions ($r < r_c$). This model was introduced to account for the sharply peaked surface brightness in the centers of relaxed X-ray systems. This model has now been widely used for both low-redshift (e.g., Pratt & Arnaud 2002) and high-redshift (e.g., Kotov & Vikhlinin 2005) clusters. It is preferred with respect to the double-β model (e.g., Mohr et al. 1999) because the two models give fits of comparable quality, while the cusped β model has one less free parameter. The cusped β model is also better behaved in the mass determination using the nonparametric method defined above (eq. [3]).

6.2. *Temperature Models*

The projected temperature profiles for our groups show a large degree of similarity. We adopted several parameterizations that have enough flexibility for each system to describe the temperature profile reasonably well and to explore the sensitivity of our results to the particular functional form. The analytic models we construct are the following:

1. Smoothly joined power laws:

$$T(r) = \frac{1}{(\{1/[t_1(r)]\}^s + \{1/[t_2(r)]\}^s)^{1/s}},$$
$$t_i(r) = T_{i,100}\left(\frac{r}{100\ {\rm kpc}}\right)^{p_i}, \quad i = 1, 2. \tag{4}$$

2. Power laws mediated by an exponential:

$$T(r) = T_0 + t_1(r)e^{-(r/r_p)^\gamma} + t_2(r)\left(1 - e^{-(r/r_p)^\gamma}\right),$$
$$t_i(r) = T_i\left(\frac{r}{r_0}\right)^{p_i}, \quad i = 1, 2. \tag{5}$$

3. The Allen et al. (2001) rising profile joined to a falling temperature profile by an exponential cutoff,

$$T(r) = t_1(r)e^{-(r/r_p)^\gamma} + t_2(r)\left(1 - e^{-(r/r_p)^\gamma}\right),$$
$$t_1(r) = a + T_1\left[\frac{(r/r_1)^{p_1}}{1 + (r/r_1)^{p_1}}\right],$$
$$t_2(r) = b + T_2\left[\frac{1}{1 + (r/r_2)^{p_2}}\right]. \tag{6}$$

The third ("RiseFall") model has been adopted in particular for temperature profiles showing an inner core flattening like NGC 533, NGC 4325, and NGC 5044, while the first two models provide comparable fits to the general profile. We assess how different choices of temperature profile, together with density profiles, affect our mass measurements in § 9.5.

6.3. *Mass Models*

We compute the total gravitating mass as the sum of DM, stars, and hot gas: $M_{\rm DM} + M_{\rm stars} + M_{\rm gas}$. For this study we only consider the contribution of the central galaxy to the stellar mass. The X-ray data provide a direct measurement of the hot gas density and therefore of $M_{\rm gas}$. We tested the following mass models against the data:

1. $M_{\rm DM} = {\rm NFW}$, $M_{\rm stars} = 0$: A single NFW model to investigate scenarios like the ones of Loeb & Peebles (2003) and El-Zant et al. (2004) and the effect of the omission of the stellar mass, if present, on the derived concentration parameter.

2. $M_{\rm DM} = {\rm NFW}$, $M_{\rm stars} = {\rm deV}$: An NFW model plus a model for a stellar component. We adopted a de Vaucouleurs stellar mass potential using the analytical approximation to the deprojected Sérsic model of Prugniel & Simien (1997) with $n = 4$. The

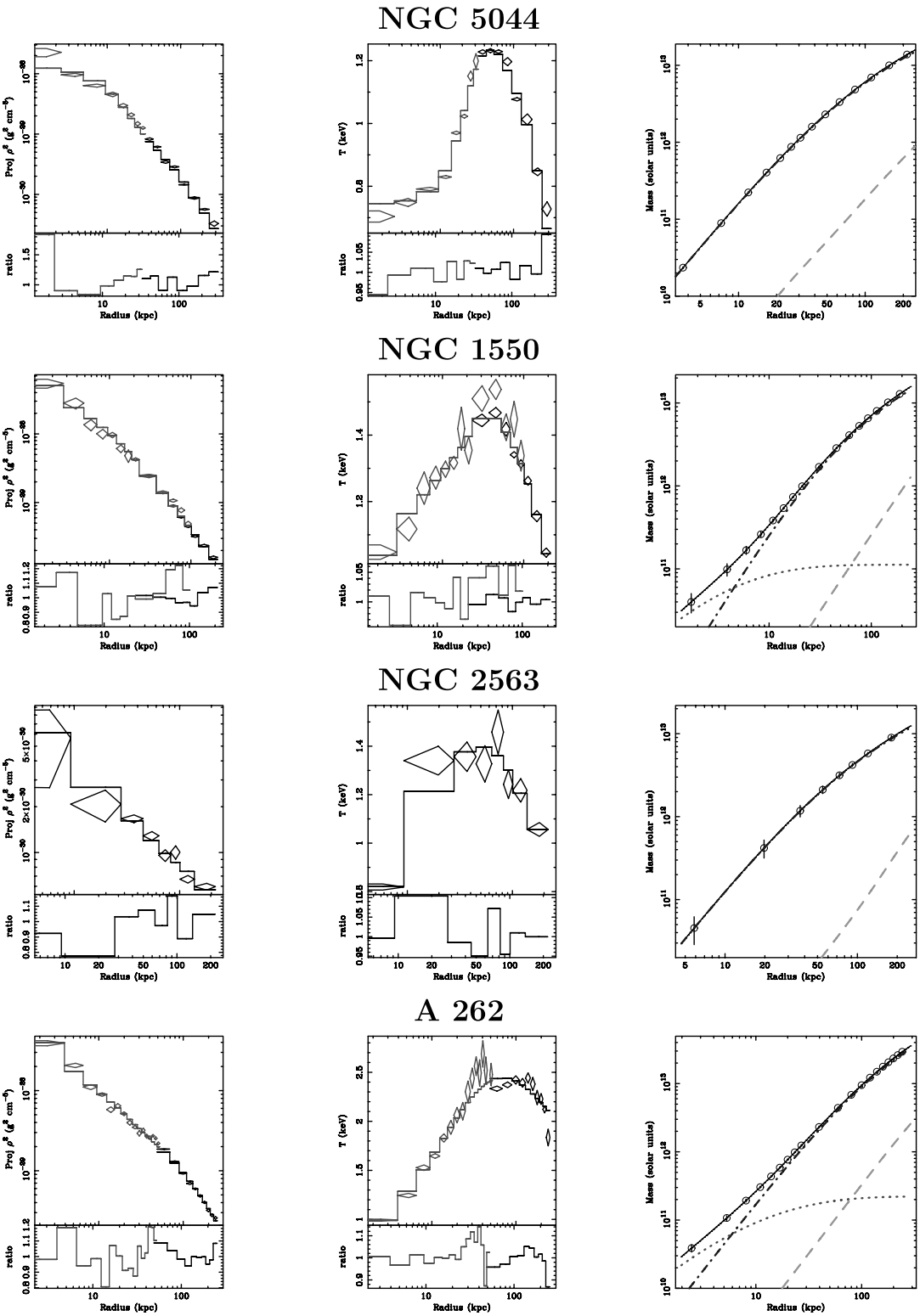

FIG. 3.—Results for the emission-weighted projection of the gas density squared (*left*), the emission-weighted projected temperature (*middle*), and the total gravitating mass (*right*) for NGC 5044, NGC 1550, NGC 2563, and A262. In the temperature and density plots, gray symbols correspond to *Chandra* data, while black symbols correspond to *XMM-Newton* data. Residuals from the best-fit parametric mass method models (§ 6) for NFW(+stars) are also shown. In the gravitating mass plot the different mass components are shown: DM with the dotted line, gas mass with the dashed line, and stellar mass with the dotted line. Representative "data points" are plotted in the gravitating mass profile to show the size of the error bars on the total gravitating mass. [*See the electronic edition of the Journal for a color version of this figure*.]

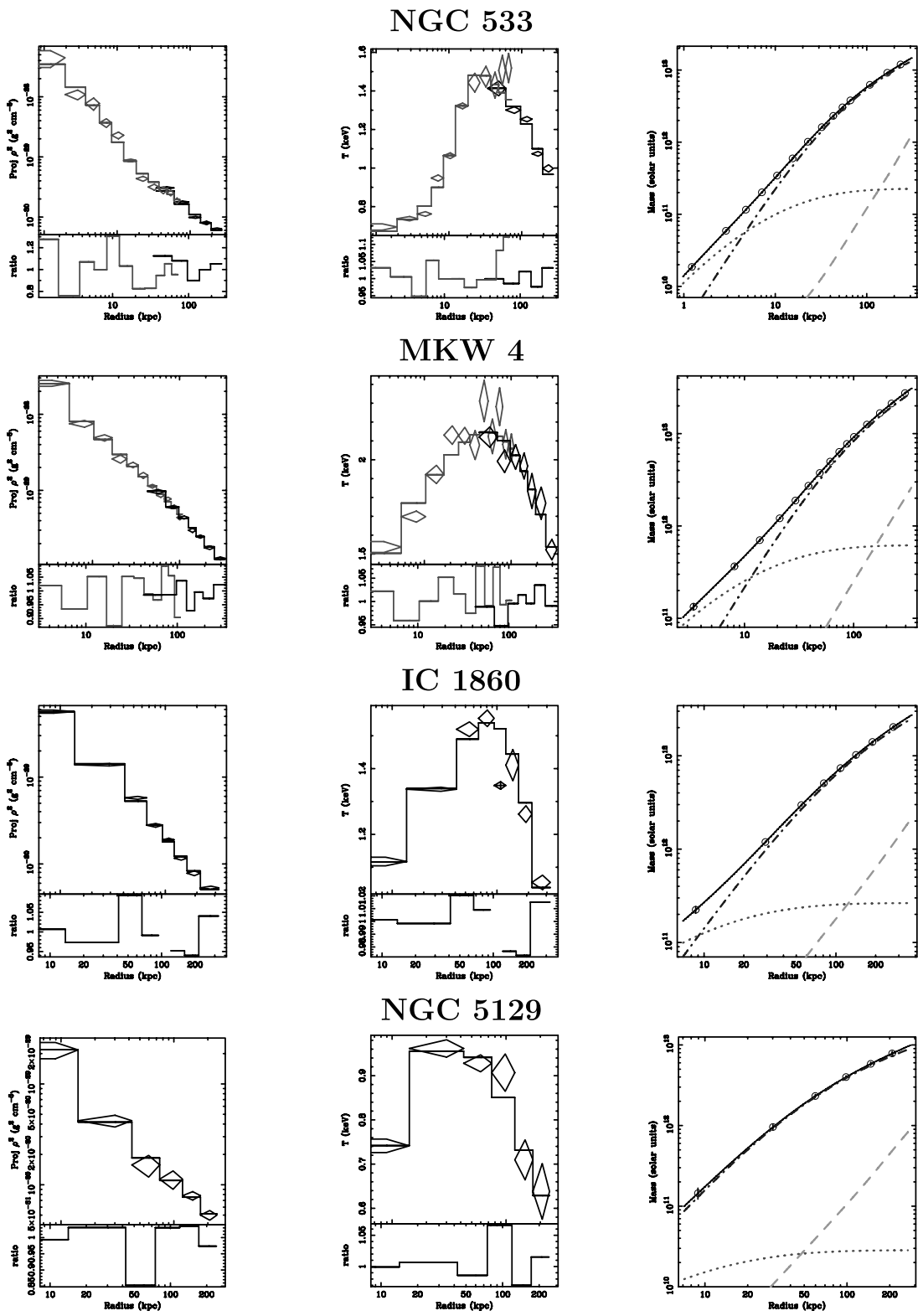

FIG. 4.— Same as Fig. 3, but for NGC 533, MKW 4, IC 1860, and NGC 5129. The crossed values for the annular bin around 100 kpc for IC 1860 indicate that the data point has not been considered in the fit. [*See the electronic edition of the Journal for a color version of this figure.*]

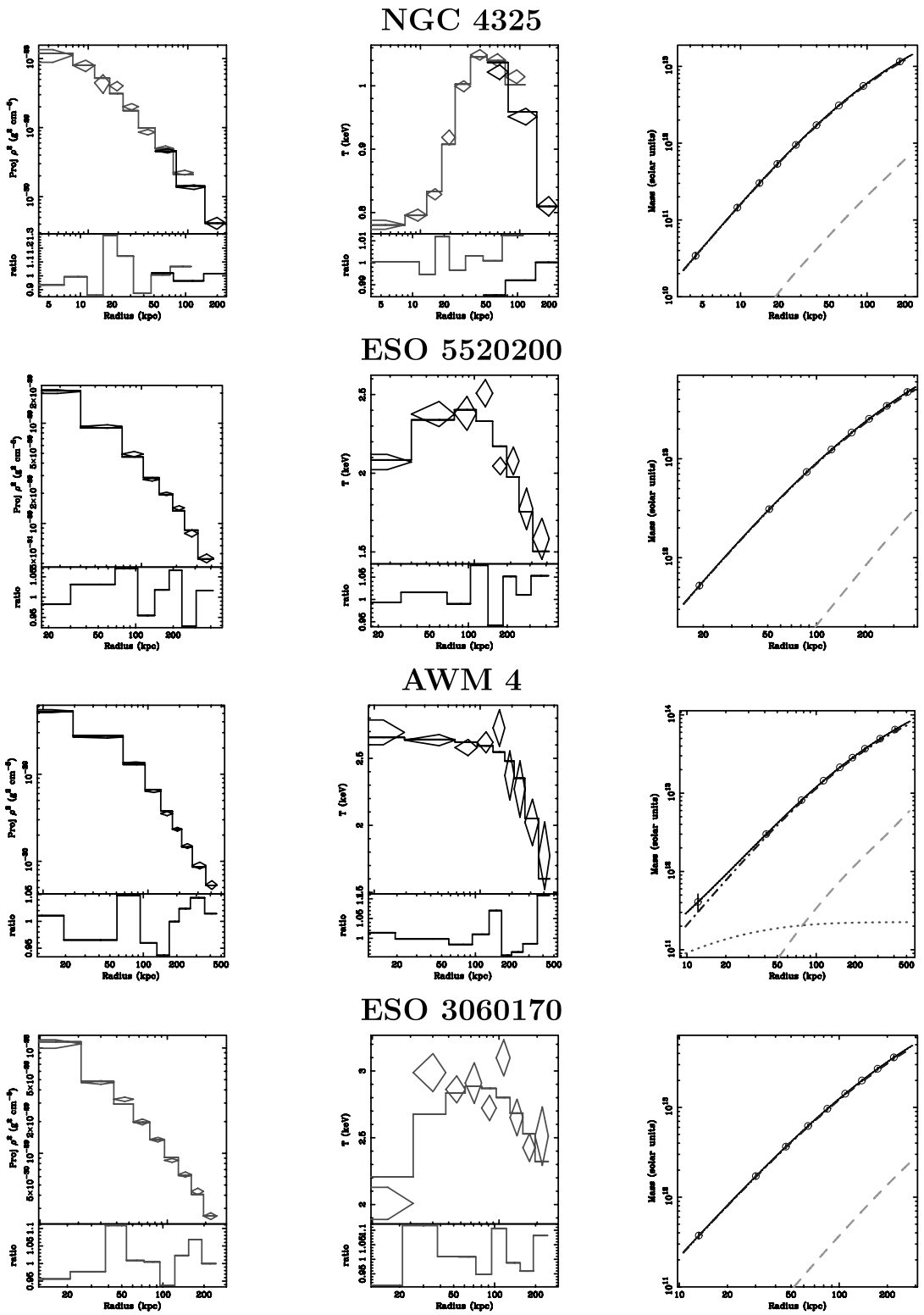

FIG. 5.—Same as Fig. 3, but for NGC 4325, ESO 5520200, AWM 4, and ESO 3060170. [*See the electronic edition of the Journal for a color version of this figure.*]

de Vaucouleurs profile is a good description of the stellar light distribution even for objects that follow the more general Sérsic profile with Sérsic index $n \neq 4$ (see Appendix A of Padmanabhan et al. 2004). The de Vaucouleurs effective radius r_e is measured in the K band by the Two Micron All Sky Survey (2MASS) as listed in the Extended Source Catalog (Jarrett et al. 2000; see Table 2). We refer to this model as NFW+stars.

3. $M_{\rm DM} = {\rm NFW}^*{\rm AC}$, $M_{\rm stars} = {\rm deV}$: An NFW component modified by the adiabatic contraction model of Gnedin et al. (2004)[5] plus a de Vaucouleurs component for the stellar mass, to explore the importance of baryon condensation in the central

[5] The adiabatic contraction code we used was made publicly available by Oleg Gnedin at http://www.astronomy.ohio-state.edu/~ognedin/contra/.

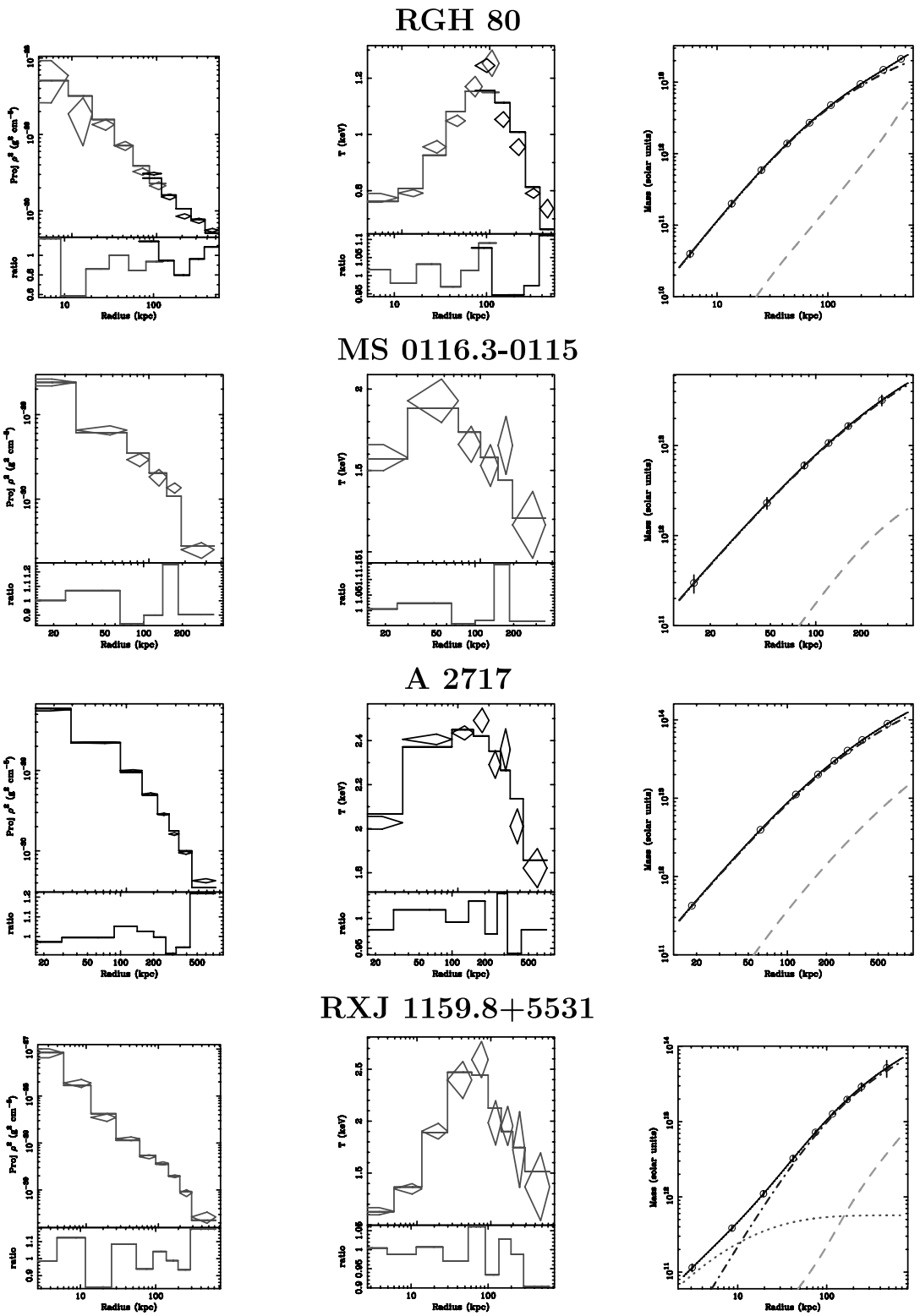

FIG. 6.— Same as Fig. 3, but for RGH 80, MS 0116.3−0115, A2717, and RX J1159.8+5531. [*See the electronic edition of the Journal for a color version of this figure.*]

galaxy for the DM halo profile. We refer to this model as NFW*AC+stars.

4. Finally, we also examined the recently suggested Sérsic-like profile (Navarro et al. 2004, hereafter N04), which should be a better parameterization of the innermost regions of CDM halos.

To obtain the true virial radius and virial mass (and concentration), we initially take r_Δ and M_Δ obtained for the DM component, where Δ corresponds to the overdensity level (2500, 1250, 500) closest to the radial range covered by the data and listed in Table 3. Then we added $M_{\rm gas}$ and $M_{\rm stars}$ to $M_{\rm DM}$ to give a new M_Δ. A new r_Δ is then computed, and the process repeated, until r_Δ changes by $<0.001\%$. (We note that in our previous studies by Humphrey et al. [2006] and Zappacosta et al. [2006] we also computed the virial radius appropriate for all of the mass components.) The values thus obtained have then been

TABLE 2
Optical Properties of the Group Central Galaxy

Name	Group	r_e/B (kpc/arcsec)	r_e/K (kpc/arcsec)	L_B ($10^{10}\ L_\odot$)	L_K ($10^{11}\ L_\odot$)
NGC 5044	NGC 5044	...	4.53/24.5	6.98	2.87
NGC 1550	NGC 1550	6.45/25.5	3.05/12.1	4.33	2.09
NGC 2563	NGC 2563	5.89/19.3	3.73/12.2	3.84	2.66
NGC 708	A262	25.60/77.1	10.16/30.6	3.84	4.12
NGC 533	NGC 533	16.92/45.4	9.22/25.2	12.4	6.14
NGC 4073	MKW 4	19.24/47.5	10.25/25.3	13.7	7.18
IC 1860	IC 1860	8.34/18.5	8.03/17.8	6.08	4.38
NGC 5129	NGC 5129	13.34/28.7	6.60/14.2	12.0	4.99
NGC 4325	NGC 4325	...	5.22/10.1	4.61	2.33
ESO 552-020	ESO 5520200	...	15.7/25.0	15.6	8.19
NGC 6051	AWM 4	10.21/16.1	10.33/16.3	9.91	7.50
ESO 306-017	ESO 3060170	...	18.51/26.0	18.5	6.95
MCG +6-29-77	RGH 80	...	5.11/6.8	...	2.93
MCG +6-29-78	RGH 80	...	6.23/8.3	4.21	2.39
UGC 842	MS 0116.3−0115	...	9.69/10.9	9.29	5.77
ESO 349-22	A2717	...	15.53/16.2	9.20	5.42
2MASSX J11595215	RX J1159.8+5531	...	9.77/6.4	23.6	10.3

Notes.—The optical properties of the central galaxy of each group. L_B was obtained from Leda, r_e in the B band from RC3 (de Vaucouleurs et al. 1991), L_K (using the luminosity distance of Table 1) and r_e in the K band from 2MASS.

converted to various overdensities (in particular the virial overdensity, listed for each object in Table 1) in Appendix A by using the formula provided by Hu & Kravtsov (2003) appropriate for an NFW halo. We prefer this procedure for extrapolating the mass and concentration to $\Delta \approx 101$ (for comparison with theoretical models) because it does not involve also extrapolating $M_{\rm gas}$. We find that the extrapolated values for the gas mass are sensitive to the radial range over which the density profile is fitted (see § 9.7).

7. RESULTS

7.1. *Mass-fitting Results*

We tested the different mass models listed in § 6.3 against the data. In the following analysis we obtain the best fit by minimizing χ^2. Although our best-fit models are not formally acceptable, the major contributions to χ^2 stem generally from the inner data points ($\lesssim$10 kpc), where the errors in both temperature and density are small. It is not expected that the DM halo of each system will be perfectly fitted by an NFW profile (e.g., Tasitsiomi et al. 2004). Consequently, we also quote the values of the maximum fractional deviation $\mathrm{dvi_{max}}$, which gives equal weight to all radial bins, as a figure of goodness of fit, in addition to χ^2 in Table 4. The quantity $\mathrm{dvi_{max}}$ is routinely used in the fits to halos formed in numerical simulations; e.g., Jing (2000) proposes that $\mathrm{dvi_{max}} < 0.30$ represents a good fit of the NFW model. The results for the best-fit NFW or NFW+stars model are listed in Table 3 at the appropriate overdensity covered by the data.

Our basic result is that the NFW model, sometimes benefiting from an additional component from the stellar mass in the central galaxy, is a good overall description of the mass profiles. While the formal quality of the fits, as noted above, is generally not

TABLE 3
Results for the NFW Fits at Selected Overdensity

Group	Δ	r_s (kpc)	c_Δ	r_Δ (kpc)	M_Δ ($10^{13}\ M_\odot$)	$M_{\rm gas,\Delta}$ ($10^{12}\ M_\odot$)	$f_{\rm gas,\Delta}$	$M_{\rm DM,\Delta}$ ($10^{13}\ M_\odot$)	$M_{\star,\Delta}$ ($10^{10}\ M_\odot$)
NGC 5044	1250	77 ± 2	3.8 ± 0.1	295 ± 2	1.85 ± 0.04	1.21 ± 0.02	0.065 ± 0.001	1.72 ± 0.04	...
NGC 1550	2500	48 ± 4	4.5 ± 0.3	215 ± 2	1.42 ± 0.03	1.02 ± 0.02	0.072 ± 0.001	1.31 ± 0.03	11.2 ± 4.1
NGC 2563	2500	76 ± 22	2.4 ± 1.0	185 ± 5	0.92 ± 0.08	0.31 ± 0.03	0.034 ± 0.001	0.89 ± 0.08	...
A262	2500	141 ± 16	2.1 ± 0.2	292 ± 4	3.59 ± 0.14	2.60 ± 0.08	0.072 ± 0.001	3.31 ± 0.13	22.1 ± 4.5
NGC 533	1250	43 ± 4	6.1 ± 0.5	262 ± 2	1.30 ± 0.04	0.87 ± 0.02	0.067 ± 0.001	1.19 ± 0.04	22.4 ± 2.2
MKW 4	1250	81 ± 7	4.3 ± 0.3	353 ± 4	3.21 ± 0.10	2.84 ± 0.06	0.088 ± 0.002	2.87 ± 0.10	61.8 ± 7.2
IC 1860	1250	101 ± 12	3.2 ± 0.3	319 ± 6	2.36 ± 0.13	1.56 ± 0.05	0.066 ± 0.002	2.18 ± 0.12	26.4 ± 6.3
NGC 5129	1250	43 ± 10	5.2 ± 0.9	226 ± 7	0.84 ± 0.07	0.58 ± 0.06	0.069 ± 0.003	0.78 ± 0.07	$2.8^{+6.7}_{-2.8}$
NGC 4325	2500	75 ± 18	2.8 ± 0.4	208 ± 8	1.32 ± 0.16	0.66 ± 0.03	0.050 ± 0.004	1.26 ± 0.16	...
ESO 5526020	1250	171 ± 27	2.5 ± 0.3	422 ± 13	5.51 ± 0.51	3.35 ± 0.18	0.061 ± 0.002	5.17 ± 0.50	...
AWM 4	1250	154 ± 17	3.0 ± 0.3	465 ± 13	7.38 ± 0.61	4.79 ± 0.29	0.065 ± 0.003	6.88 ± 0.59	$22.5^{+24.7}_{-22.5}$
ESO 3060170	2500	162 ± 54	2.1 ± 0.3	343 ± 18	5.97 ± 1.14	3.45 ± 0.17	0.058 ± 0.005	5.62 ± 1.12	...
RGH 80	500	78 ± 8	5.1 ± 0.5	397 ± 5	1.85 ± 0.07	2.85 ± 0.11	0.154 ± 0.003	1.56 ± 0.06	...
MS 0116.3−0115	1250	202 ± 115	2.0 ± 0.8	405 ± 42	4.92 ± 1.64	1.97 ± 0.19	0.040 ± 0.009	4.73 ± 1.63	...
A2717	500	233 ± 18	3.0 ± 0.2	710 ± 11	10.68 ± 0.51	11.36 ± 0.29	0.106 ± 0.003	9.55 ± 0.49	...
RX J1159.8+5531	500	104 ± 77	5.6 ± 1.5	584 ± 73	6.13 ± 3.30	5.10 ± 0.41	0.083 ± 0.019	5.57 ± 3.32	56.9 ± 10.5

Notes.—Results for the mass profile fits. Parameter Δ refers to the overdensity chosen for the object, as the closest to the outer radius of the data. Parameter r_s is the scale radius of the NFW profile.

TABLE 4
Quality of the Mass Fits

Group	χ^2 NFW(+stars)	χ^2 NFW*AC+stars	$\mathrm{dvi}_{\max}$ NFW(+stars)
NGC 5044	228/20	...	0.83
NGC 1550	66/33	74/33	0.22
NGC 2563	18/7	...	0.23
A262	116/37	134/37	0.19
NGC 533	81/20	85/20	0.30
MKW 4	34/24	63/24	0.13
IC 1860	14/5	25/5	0.11
NGC 5129	3/2	3/2	0.15
NGC 4325	12/9	...	0.29
ESO 5520200	18/8	...	0.08
AWM 4	13/9	14/9	0.11
ESO 3060170	25/9	...	0.12
RGH 80	71/9	...	0.42
MS 0116.3−0115	6/5	...	0.16
A2717	32/9	...	0.22
RX J1159.8+5531	5/7	13/7	0.17

Notes.—Various indicators of quality of fit for the mass models discussed in the text. Parameter χ^2 refers to the χ^2/dof of the fits to the density and temperature profiles used to infer the parameters of the mass model in the gas potential approach. Parameter $\mathrm{dvi}_{\max}$ refers to the maximum fractional deviation on the fits to the density and temperature profiles used to infer the parameters of the mass model in the gas potential approach. Values of χ^2 for the NFW*AC+stars model are reported only for the objects showing an excess over the NFW fit due to stellar mass.

TABLE 5
Stellar Mass-to-Light Ratios

Galaxy	L_K/L_B	Fitted M_*/L_K ($M_\odot\ L_\odot^{-1}$) NFW+H90	Fitted M_*/L_K ($M_\odot\ L_\odot^{-1}$) NFW*AC+H90
NGC 1550	4.8	0.53 ± 0.20	0.24 ± 0.01
NGC 708	10.7	0.54 ± 0.11	0.14 ± 0.10
NGC 533	4.9	0.36 ± 0.03	0.11 ± 0.01
NGC 4073	4.6	0.86 ± 0.10	0.33 ± 0.04
IC 1860	7.2	0.60 ± 0.14	0.26 ± 0.01
NGC 5129	4.1	$0.06^{+0.13}_{-0.06}$	0.05 ± 0.01
NGC 6051	7.6	$0.30^{+0.33}_{-0.30}$	0.18 ± 0.01
2MASSX J11595215	4.4	0.55 ± 0.10	0.40 ± 0.05

Note.—K-band stellar mass-to-light ratios for the central galaxy measured from our fits to the data using the NFW+stars and the NFW*AC+stars models.

acceptable, the fractional deviations of the fits are typically ∼10%. The largest maximum deviation is observed for NGC 5044 within its central radial bin (<3 kpc), where the *Chandra* image shows irregularities presumably associated with AGN feedback (Buote et al. 2003). At all other radii the deviations are ≲10% for NGC 5044.

The stellar mass component is not uniformly required. When using the NFW+stars model, only 8 objects of the 16 in the sample show an improvement in the fit. The improvement of the fit is judged by considering a reduction in χ^2 and a reduction in fractional residuals. This provides a quantitative assessment of the improvement of the fit even if the final χ^2 is still not formally acceptable. For example, an NFW fit to the MKW 4 mass profile gives $\chi^2/\mathrm{dof} = 58/25$ with a $\mathrm{dvi}_{\max}$ of 0.60 arising from the central density bin, while the best-fit NFW+stars gives $\chi^2/\mathrm{dof} = 34/24$ with a $\mathrm{dvi}_{\max}$ of 0.13 because the inner data points are better modeled.

Moreover, the amount of improvement is sensitive both to the number of data points sampling the inner ≈20 kpc (where the stellar mass is expected to make a substantial contribution to the total mass budget) and to the luminosity of the central galaxy. For this purpose it is instructive to examine those systems that require stellar mass and have both *Chandra* and *XMM-Newton* data: NGC 1550, A262, NGC 533, and MKW 4. By fitting only the *XMM-Newton* data, with its coarser binning at small radius, we can assess the importance of having high-resolution *Chandra* data for detecting a stellar mass component. When fitting only the *XMM-Newton* data for these systems, the evidence for a stellar mass component is weaker, and the inferred amount of stellar mass less, than for the simultaneous *Chandra*/*XMM-Newton* fits. The amount of stellar mass inferred is always larger when the *Chandra* data are included. In three of the four cases, the derived concentration value does not change within the $1-2\ \sigma$ errors. The exception is A262, for which $c_\Delta = 1.2 \pm 0.1$ is obtained using only *XMM-Newton* and $c_\Delta = 2.1 \pm 0.2$ is found for the simultaneous *Chandra*/*XMM-Newton* fits.

It follows that for systems having only *XMM-Newton* data it is necessary to obtain high-quality *Chandra* observations to make a reliable detection of stellar mass. There is clear failure to detect stellar mass in three objects in our sample that are adequately sampled by *Chandra* observations: NGC 5044, NGC 4325, and RGH 80.

The omission of the stellar component in the mass fits leads to biased high concentrations (Mamon & Łokas 2005; Humphrey et al. 2006), but the relevance of the bias depends on the number of data points sampling both the stellar component (dominant in the inner ∼20 kpc) and DM component. The objects in our sample have adequate sampling of the DM component at relatively large radii, but the stellar component is well sampled (∼3 data bins in the inner 20 kpc) only when *Chandra* data are present. As a consequence, the bias is more pronounced when *Chandra* data are included. This effect is most evident for MKW 4. An NFW fit to the *XMM-Newton* data for MKW 4 gives $c_\Delta = 5.8 \pm 0.3$, while an NFW+stars fit gives $c_\Delta = 4.8 \pm 0.4$. If we use *Chandra* and *XMM-Newton* data, then the fit is driven by the increased number of data points within 20 kpc. Fitting an NFW model yields $c_\Delta = 6.8 \pm 0.2$, which represents a 58% increase over our best-fit NFW+stars value, $c_\Delta = 4.3 \pm 0.3$ (see Table 3). For the remaining objects, fitting only the NFW model, when NFW+stars is required, returns a c_Δ biased high in the range from 38% (A262) to 10% (NGC 533). As expected, the bias is generally less for our groups-clusters ($M > 10^{13}\ M_\odot$) than obtained for the elliptical galaxies–groups ($M \lesssim 10^{13}\ M_\odot$) analyzed by Humphrey et al. (2006).

In order to explore the presence and relevance of adiabatic contraction, we fitted an NFW*AC+stars model to the eight objects that require a stellar mass component because only for these objects is the AC model potentially relevant. The quality of the fits is not improved by the introduction of AC (see Table 4). Because the AC model increases the cuspiness of the DM profile, we find that the stellar mass (and the derived stellar mass-to-light ratios; see Table 5) was considerably lower for the NFW*AC+stars model than for the NFW+stars model. Because less stellar mass is obtained for the AC models, the derived c_Δ values increase by 10%–40% compared to NFW+stars. Two exceptions are MKW 4 and RX J1159.8+5531, for which AC increases c_Δ to 7.1 ± 0.4 and 9.6 ± 1.9, respectively. The quality of the NFW*AC+stars fits is considerably worse in these two cases compared to NFW+stars. The M_Δ values obtained for the NFW*AC+stars model are also lower by 5%–20%, with a maximum of 33% for RX J1159.8+553.

Finally, we examined the N04 model. We explored N04+stars because in our previous analysis of the cluster Abell 2589 (Zappacosta et al. 2006) N04 allowed for an increased contribution

from stellar central mass components (with values of the Sérsic parameter $\alpha \sim 0.4$). Even if we left the Sérsic parameter α free, the fit improved only in a few cases, and only in two, A2717 (χ^2/dof = 7/4) and IC 1860 (χ^2/dof = 7/4), was the improvement superior to 90% according to the *F*-test. The inferred values of α for the sample were quite large and incompatible with the mean value of 0.17 ± 0.03 for CDM halos (N04). If we fixed the value of α at 0.17, the fits did not improve.

7.2. *Stellar Mass-to-Light Ratios*

Using the stellar mass derived from our fits, we calculated the stellar M/L ratios ($M_\star/L$) for the central galaxy. The optical luminosities have been calculated in the K_s band, following Kochanek et al. (2001) and Lin & Mohr (2004) using (1) the 20 mag arcsec^{-2} isophotal elliptical aperture magnitude, (2) the value of the Galactic extinction provided by NED, (3) a *k*-correction of the form $k(z) = -6 \log (1 + z)$, and (4) a correction of 0.2 mag to convert between the total and isophotal absolute magnitudes (see Appendix of Kochanek et al. 2001). We compare this estimate to the total extrapolated magnitudes listed in the Extended Catalog, finding agreement to better than 10%.[6] For distances we adopted the luminosity distance listed in Table 1. Magnitudes have been converted to units of *B* and K_s solar luminosities using $M_{B,\odot} = 5.48$ (Girardi et al. 2000) and $M_{K_s,\odot} = 3.34$, which follows from adopting $(B - V)_\odot = 0.64$ and $(V - K_s)_\odot = 1.50$ (Holmberg et al. 2006).

We use the *K* band to quote $M_\star/L$ because near-infrared (NIR) luminosities are much more closely correlated with the total galaxy mass than optical luminosities (Gavazzi et al. 1996). Table 5 shows the best-fitting results for NFW+stars and NFW*AC+stars for those objects requiring a stellar mass component in the mass analysis in § 7.1.

8. RESULTS FOR INDIVIDUAL OBJECTS

In the right panels of Figures 3, 4, 5, and 6 we show the total gravitating mass profiles for the objects in our sample, with the different components (DM, gas mass, and stellar mass of the central galaxy) shown in different shades and line styles. Details for some individual objects, as well as comparison with previous results in the literature, are provided below.

NGC 1550.—Our density and temperature profiles agree with the *Chandra* analysis of Sun et al. (2003). Their fit to the *total mass* profile within 200 kpc, not surprisingly, prefers a Moore profile over an NFW (in particular in the inner 10 kpc) because of the stellar mass contribution, which steepens the profile of the total gravitating matter. Our derived DM parameters for an NFW fit are not very different from their NFW fit to the total matter: our scale radius $r_s = 48 \pm 4$ kpc and $\delta_c = (7.76 \pm 0.56) \times 10^4$ are similar to their best-fitting values of 41.8 kpc and 1.10×10^5, respectively.

Abell 262.—The total mass profile has been analyzed using both *Chandra* and *ROSAT* data at large radii by Vikhlinin et al. (2006), who find a concentration $c_{500} = 3.54 \pm 0.30$, which is consistent within 2 σ with ours (4.5 ± 0.4; see Table 7 below). Other relevant quantities are in excellent agreement: our values of $M_{2500} = (3.59 \pm 0.14) \times 10^{13}\, M_\odot$, $f_{\rm gas,2500} = 0.072 \pm 0.001$, and $r_{500} = 624 \pm 15$ kpc agree well with their values of $(3.40 \pm 0.50) \times 10^{13}\ M_\odot$, 0.067 ± 0.003, and 650 ± 21 kpc. Using *XMM-Newton* data, Piffaretti et al. (2005) obtained the following parameters from a single NFW model fitted to the gravitating matter: $r_s = 85 \pm 17$ kpc, $c_{200} = 8.6 \pm 1.0$, $M_{\rm DM,2500} = (1.97 \pm 0.27) \times 10^{13}\, M_\odot$, and $M_{\rm gas,2500} = (1.36 \pm 0.20) \times 10^{12}\, M_\odot$. These values do not agree with ours, even when we similarly fit only the NFW model (i.e., no separate accounting for stars or gas) to the *XMM-Newton* data: $r_s = 174 \pm 10$ kpc, $M_{\rm DM,2500} = (3.39 \pm 0.10) \times 10^{13}\, M_\odot$, and $M_{\rm gas,2500} = (2.76 \pm 0.06) \times 10^{12}\, M_\odot$. Considering the agreement between our results and those of Vikhlinin et al. (2006), it is unclear why Piffaretti et al. (2005) obtain different results for this system.

NGC 533.—Using *XMM-Newton* data, Piffaretti et al. (2005) obtain the following results for the NFW model fitted to the gravitating mass: $r_s = 37 \pm 3$ kpc and $c_{200} = 12.53 \pm 0.55$. Under the same conditions we obtain good agreement with their results: $r_s = 43 \pm 4$ kpc and $c_{200} = 13.0 \pm 0.9$.

MKW 4.—Our derived temperature profile shows a declining behavior like the one obtained by Vikhlinin et al. (2005) using *Chandra* data, by Fukazawa et al. (2004) using both *Chandra* and *XMM-Newton* data, and by Finoguenov et al. (2007) using *XMM-Newton* data. However, our profile does not agree with the relatively flat profile with higher temperature values obtained by O'Sullivan et al. (2003). We believe that the origin of the discrepancy probably arises from their application of the double subtraction method to subtract the background (§ 3.3) because the emission from MKW 4 fills the entire *XMM-Newton* field of view. The subtraction of a source component artificially hardens the outermost annuli. A similar conclusion has been reached by Finoguenov et al. (2007). Our mass model extrapolated to $\Delta = 500$ gives $c_{500} = 6.4 \pm 0.5$, $r_{500} = 527 \pm 8$ kpc, and $M_{500} = (4.27 \pm 0.18) \times 10^{13}\, M_\odot$, which do not agree with the parameters found by Vikhlinin et al. (2006), $c_{500} = 2.54 \pm 0.15$, $r_{500} = 634 \pm 28$ kpc, and $M_{500} = (7.7 \pm 1.0) \times 10^{13}\ M_\odot$, obtained by combining *Chandra* and *ROSAT* data at large radii (out to 550 kpc). However, when restricting the comparison to the radial range covered by our data, our mass [$M_{2500} = (2.4 \pm 0.1) \times 10^{13}\ M_\odot$] agrees with theirs [$M_{2500} = (2.8 \pm 0.3) \times 10^{13}\ M_\odot$]. The difference in concentrations stems primarily from a difference between our measured scale radius, $r_s = 81 \pm 7$ kpc, and their value of 250 kpc. As we discuss in § 9.7, a measurement of the scale radius is reliable only if it is well within the radial range of the data. Although by using *ROSAT* data Vikhlinin et al. (2006) have surface brightness information out to 550 kpc, accurate spectral information is available only with *Chandra* data, which beyond $\sim$100 kpc (outside of the ACIS-S3 chip) are only covering a sector of the entire radial annulus and have relatively low S/N. The similar scale radius of 76 kpc for this object derived by Rines & Diaferio (2006) using galaxy redshifts and identifying caustics in redshift space supports our results, although the value of $r_{500} = 620$ kpc agrees better with Vikhlinin et al. (2006) (634 ± 28 kpc) than with the present work (527 ± 8 kpc). Other possible reasons for the discrepancy are the different mass modeling procedure or the different radial range used in the fit, restricted to $r > 37$ kpc in the analysis of Vikhlinin et al. (2006).

IC 1860.—The group exhibits a sharp decline in surface brightness in the northwest and enhanced emission in the southeast. This particularly affects the annulus between 94 and 121 kpc, which has been excluded from the fit. We studied the effects of this asymmetry by dividing the annuli into two sectors. We defined the southeast sector as 15°–195° measured from the north. The corresponding northwest sector is then 195°–15°. We find that the gas density profile is steeper in the northwest direction, but the lower temperature in the 91–125 kpc annulus is caused by the cooler, higher density emission in the southeast. The radial

[6] For a discussion regarding the use of the elliptical isophotal magnitude instead of the extrapolated total magnitude, because it is less vulnerable to stellar contamination and surface brightness irregularities, see the FAQ sheet for the 2MASS Extended Source Catalog at http://spider.ipac.caltech.edu/staff/jarrett/2mass/XSC/jarrett_XSCprimer.html.

temperature profile is quite smooth over the northwest sector. The c_Δ and M_Δ values obtained for each sector when excluding the 94–121 kpc annulus are consistent within their $\sim 2\ \sigma$ errors. Including this annulus has negligible impact on the results for the northwest sector. These low-level disturbances did not indicate a significant violation of hydrostatic equilibrium, as further suggested by the agreement of the derived $c_{\rm vir}$ and $M_{\rm vir}$ with the values expected from ΛCDM simulation.

NGC 4325.—We measured an NFW scale radius $r_s = 75 \pm 18$ kpc and $M_{200} = (3.01 \pm 0.65) \times 10^{13}\ M_\odot$. The results agree with the uncertain values obtained by Rines & Diaferio (2006), i.e., $M_{200} = (1.5 \pm 1.3) \times 10^{13}\ M_\odot$ and $r_s = 82$ kpc.

AWM 4.—This object has a remarkable temperature profile. Unlike the other groups in our sample, the core is isothermal as found previously by O'Sullivan et al. (2005). Beyond a radius of 200 kpc we measure a declining temperature profile with the *XMM-Newton* data. We find that the source emission fills the entire field of view, contrary to the analysis in O'Sullivan et al. (2005), which reported a "soft excess" described by a 0.6 keV bremsstrahlung component, probably the misinterpreted source. It is difficult to classify AWM 4 as a merging system, given its relaxed appearance both in the X-rays and in the optical (Koranyi & Geller 2002). Instead, the flat temperature profile likely reflects the influence of the powerful AGN, with radio lobes extending out from the central galaxy NGC 6051 along the minor axis of the galaxy to 100 kpc (e.g., Neumann et al. 1994).

ESO 3060170.—Our temperature profile is best fitted by a declining profile at large radii. However, because of the relatively large error bars, our profile is also consistent with the flat profile obtained by Sun et al. (2004) between 10 and 400 kpc with *XMM-Newton* and *Chandra*. Sun et al. (2004) obtain $c_{200} \sim 8.7$ and $M_{200} \sim 1.8 \times 10^{13}\ M_\odot$, which may be compared to our extrapolated values, $c_{200} = 6.7 \pm 0.8$ and $M_{200} = (1.54 \pm 0.59) \times 10^{14}\ M_\odot$.

RGH 80.—The *Chandra* image clearly reveals the peak of the X-ray emission coincident with MCG +06-29-077 and a bright tail pointing northwest, with MCG +06-29-078 at the south edge of this feature. This geometry was only hinted at by the *XMM-Newton* image (see Fig. 10 of Mahdavi et al. 2005). This asymmetry is an indication that the core is not fully relaxed, as already suggested by the absence of a single central galaxy. Despite this fact, hydrostatic equilibrium beyond the inner core seems a good approximation given the values of $c_{\rm vir}$ and $M_{\rm vir}$ measured for this object.

Abell 2717.—The temperature profile we have derived from *XMM-Newton* data declines at large radii, like all of the groups in our sample, and is inconsistent with the flat profile found by Pratt & Arnaud (2005). The origin of the difference is likely our improved treatment of background subtraction. Nevertheless, our inferred $c_{200} = 4.6 \pm 0.2$, $M_{200} = (1.59 \pm 0.06) \times 10^{14}\ M_\odot$, and $r_{200} = 1082 \pm 21$ are in good agreement with those determined by both Pratt & Arnaud (2005) and Pointecouteau et al. (2005), $c_{200} = 4.21 \pm 0.25$, $M_{200} = (1.57 \pm 0.19) \times 10^{14}\ M_\odot$, and $r_{200} = 1096 \pm 44$. The reason for the agreement, despite the difference in the temperature profiles, is likely the same put forward by Vikhlinin et al. (2006): the NFW fit implies a declining temperature profile at large radii.

RX J1159+5531.—Our inferred $c_{500} = 5.6 \pm 1.5$ is higher than the one reported in Vikhlinin et al. (2006), $c_{500} = 1.7 \pm 0.3$, using the same *Chandra* data, although within $2.5\ \sigma$ given our large error bars. Our derived $M_{2500} = (3.3 \pm 0.9) \times 10^{13}\ M_\odot$ and gas fraction $f_{\rm gas,2500} = 0.049 \pm 0.004$ are, on the contrary, in good agreement with their determination of $(3.0 \pm 0.3) \times 10^{13}\ M_\odot$ and 0.045 ± 0.002. As for MKW 4, the key difference is in the measured scale radius: our value of 104 ± 77, although with large error bars, is inconsistent with their quite high value of 412 kpc, which is again at the boundary of the radial range covered by the data, which are of not excellent quality outside the S3 chip (∼370 kpc).

9. SYSTEMATIC ERRORS

In this section we address the sensitivity of our analysis to various systematic uncertainties and data analysis choices that may impact our results. An estimate of the uncertainty due to these effects for each object is given in Table 6. The statistical error of the default model (ΔStatistical) is also listed on the table. In the case of the different approach of using a deprojection technique (ΔDeproj), we also quote the corresponding magnitude of statistical error together with the associated best-fitting parameter shift in the table. We illustrate the effect of systematic errors on the best-fit c_Δ and M_Δ parameters and the stellar mass-to-light ratio $M_\star/L_K$.

9.1. *Background Modeling and Subtraction*

One of the most important potential sources of systematic uncertainties in measuring the mass profiles of groups is the background subtraction technique, in particular in the low surface brightness regime at large radii. Our modeling technique is particularly effective in the low-temperature regime of groups. We changed the overall normalization of the background model by ±5%; such an error in the estimated background is unlikely, but the exercise is indicative of our sensitivity to the background.

9.2. *Spectral Fitting Choices*

Among the variety of choices made in spectral fitting, we explore the ones more likely to affect to some degree the inferred gas density and temperature in each radial bin.

The plasma code.—Different plasma codes choose from a large, overlapping, but incomplete set of atomic data, leading to differences in the inferred abundances and, therefore, density and, to a lesser extent, temperature. We experimented with replacing the APEC model with the MEKAL plasma model.

Bandwidth.—To estimate the impact of the bandwidth on our fits, we experimented with fitting the data with different lower limits for the energy band. In addition to our preferred choice of 0.5 keV, we use 0.4 and 0.7 keV.

Hydrogen column density.—We take into account possible deviations for $N_{\rm H}$ from the value of Dickey & Lockman (1990), allowing the parameter to vary by ±25%.

9.3. *Deprojection Method*

We analyzed the possible systematics involved with the projection of 3D models using instead the "onion-peeling" technique (e.g., Fabian et al. 1981; Kriss et al. 1983; Buote 2000a). Only for the object IC 1860 did we not perform this exercise because of the exclusion of an inner bin (see § 8). The results were consistent with the ones obtained by the 2D analysis (see Table 6), but with larger error bars given the quality of the current data. This is the main reason for having adopted the 2D analysis as our default. In Figure 7 we plot as a function of the fraction of the virial radius the quantity $\Delta\rho/\rho_{\rm 3D}$ (where $\Delta\rho = \rho_{\rm 2D} - \rho_{\rm 3D}$, with $\rho_{\rm 2D}$ the value of the best-fit model of the 2D analysis) and the corresponding quantity $\Delta T/T_{\rm 3D}$. The plotted errors are the fractional errors on the derived 3D quantities. There is more scatter in the density as a consequence of larger uncertainties in the derived 3D iron abundances, while the temperatures determined with the two methods are generally consistent. This fact reinforces the notion that, for the range of temperatures spanned by the objects considered in

TABLE 6
SYSTEMATIC ERROR BUDGET

Group	Best Fit	ΔStatistical	ΔBackground	ΔSpectral	ΔMethod	ΔDeproj	Δr_e
			c_Δ				
NGC 5044	3.8	±0.1	−0.5	+0.2	+0.6	−0.3 (±0.2)	...
NGC 1550	4.5	±0.3	+0.4	±0.2	−0.1	−0.8 (±0.3)	+0.5
NGC 2563	2.4	±1.0	+2.6	+2.3	−0.1	+4.5 (±1.4)	...
A262	2.1	±0.2	+0.2	$^{+0.8}_{-0.6}$	−0.4	−0.4 (±0.2)	−0.2
NGC 533	6.1	±0.5	−1.7	−2.0	+1.1	−1.5 (±0.4)	+0.9
MKW 4	4.3	±0.3	−0.1	$^{+0.3}_{-0.7}$	−0.3	+0.8 (±0.7)	−0.3
IC 1860	3.2	±0.3	+0.1	$^{+0.9}_{-0.4}$	−1.3	...	...
NGC 5129	5.2	±0.9	+0.6	−0.4	−0.3	−0.2 (±2.2)	...
NGC 4325	2.8	±0.4	+0.7	+0.9	+0.3	−0.7 (±0.3)	...
ESO 5520200	2.5	±0.3	−0.2	−0.3	+0.1	+0.2 (±0.4)	...
AWM 4	3.0	±0.3	+0.1	−0.2	−0.1	−0.9 (±0.3)	...
ESO 3060170	2.1	±0.3	−0.4	$^{+0.8}_{-0.6}$	−0.3	−0.1 (±0.3)	...
RGH 80	5.1	±0.5	+2.1	+4.5	−2.6	+2.9 (±1.2)	...
MS 0116.3−0115	2.0	±0.8	+0.7	$^{+1.5}_{-0.5}$	+1.0	+2.3 (±1.9)	...
A2717	3.0	±0.2	+0.1	−0.2	−0.1	+0.6 (±0.3)	...
RX J1159.8+5531	5.6	±1.5	−0.9	+0.7	−1.2	+2.6 (±1.7)	...
			$M_\Delta/10^{13}\ M_\odot$				
NGC 5044	1.85	±0.04	+0.28	−0.10	−0.41	+0.34 (±0.09)	...
NGC 1550	1.42	±0.03	−0.04	−0.03	+0.02	+0.26 (±0.09)	+0.01
NGC 2563	0.92	±0.08	−0.06	−0.17	+0.01	−0.24 (±0.13)	...
A262	3.59	±0.14	−0.19	$^{+0.24}_{-0.62}$	+0.34	+1.00 (±0.31)	+0.10
NGC 533	1.30	±0.04	$^{+0.15}_{-0.01}$	+0.16	−0.04	−0.01 (±0.07)	−0.05
MKW 4	3.21	±0.10	−0.10	$^{+0.12}_{-0.07}$	+0.09	−0.86 (±0.18)	+0.03
IC 1860	2.36	±0.13	−0.08	$^{+0.12}_{-0.20}$	+0.65	...	...
NGC 5129	0.84	±0.07	$^{+0.08}_{-0.03}$	−0.02	...	−0.13 (±0.15)	...
NGC 4325	1.32	±0.16	−0.15	−0.20	−0.10	+0.53 (±0.45)	...
ESO 5520200	5.51	±0.51	+0.35	$^{+0.70}_{-0.13}$	−0.40	+0.49 (±0.71)	...
AWM 4	7.38	±0.61	−0.27	−0.70	+0.16	+2.01 (±0.87)	...
ESO 3060170	5.97	±1.14	+1.30	$^{+2.07}_{-0.74}$	+0.73	+0.68 (±1.37)	...
RGH 80	1.85	±0.07	$^{+0.26}_{-0.14}$	$^{+0.05}_{-0.40}$	+0.48	−0.07 (±0.19)	...
MS 0116.3−0115	4.92	±1.64	+0.46	$^{+0.68}_{-1.42}$	−1.12	−0.40 (±3.76)	...
A2717	10.68	±0.51	−0.03	+1.02	+0.49	−0.76 (±0.86)	...
RX J1159.8+5531	6.13	±3.30	+0.97	−0.29	+0.51	−1.87 (±0.72)	...
			$M_\star/L_K\ (M_\odot\ L_\odot^{-1})$ (NFW+stars)				
NGC 1550	0.53	±0.20	+0.05	+0.12	+0.03	+0.17 (±0.15)	+0.36
A262	0.54	±0.11	−0.13	$^{+0.23}_{-0.37}$	+0.12	−0.45 (±0.04)	+0.79
NGC 533	0.36	±0.03	+0.20	+0.26	−0.27	+0.24 (±0.04)	−0.07
MKW 4	0.86	±0.10	$^{+0.51}_{-0.66}$	$^{+0.59}_{-0.54}$	+0.11	+0.15 (±0.09)	+0.60
IC 1860	0.60	±0.14	+0.01	$^{+0.02}_{-0.23}$	+0.53	...	...
NGC 5129	0.06	$^{+0.13}_{-0.06}$	$^{+0.13}_{-0.06}$	−0.06	+0.06	+0.43 (±0.19)	...
AWM 4	0.30	$^{+0.33}_{-0.30}$	+0.08	±0.12	+0.14	+0.82 (±0.38)	...
RX J1159.8+5531	0.55	±0.10	+0.05	$^{+0.10}_{-0.13}$	+0.11	−0.13 (±0.13)	...

NOTES.—The estimated error budget for each of the groups. Excepting the statistical error, these values estimate a likely upper bound on the sensitivity of the (best fit) value of each parameter to various data analysis choices and should *not* be added in quadrature with the statistical error. The "Best" column indicates the best-fit value and "ΔStatistical" the 1 σ statistical error for M_Δ and c_Δ from Table 3 and for $M_\star/L_K$ from Table 5. "ΔBackground" gives the results when the X-ray background level is set to ±5% of nominal, "ΔSpectral" gives the results when changing spectral analysis choices, "ΔMethod" when adopting a different approach (using eq. [2] or eq. [3]) to mass modeling, "ΔDeproj" when using projected (2D) or deprojected (3D) spectral results (with the associated statistical error), and Δr_e when changing the effective radius of the stellar profile.

this paper, the spectroscopic temperatures are not biased significantly (see discussion in §§ 9.4 and 10.5).

9.4. *Response Weighting*

Since the effective area of the detector response of ACIS on *Chandra* and EPIC on *XMM-Newton* is a decreasing function of energy, fitting a single-temperature (1T) model to a spectrum having a range of temperature components above ~3 keV will tend to yield a temperature that is biased low (Mazzotta et al. 2004; Vikhlinin 2006). This effect is negligible for average temperatures around 1 keV (see Appendix B and Buote 2000c), as it is the case for the objects in our sample. As a further systematic check, we applied a straightforward averaging of the plasma emissivity over the detector response in our method as explained in Appendix B. The results obtained using the response weighting are very consistent with the ones obtained by our default projection analysis. For example, for NGC 1550 we obtain $c_\Delta = 4.5 \pm 0.3$, $M_\Delta = (1.45 \pm 0.03) \times 10^{13}\ M_\odot$, and $M_{\star,\Delta} = (11.1 \pm 4.0) \times 10^{11}\ M_\odot$; for MKW 4 we obtain $c_\Delta = 5.1 \pm 0.4$, $M_\Delta = (2.91 \pm 0.10) \times 10^{13}\ M_\odot$, and $M_{\star,\Delta} = (60.7 \pm 7.3) \times 10^{11}\ M_\odot$; for NGC

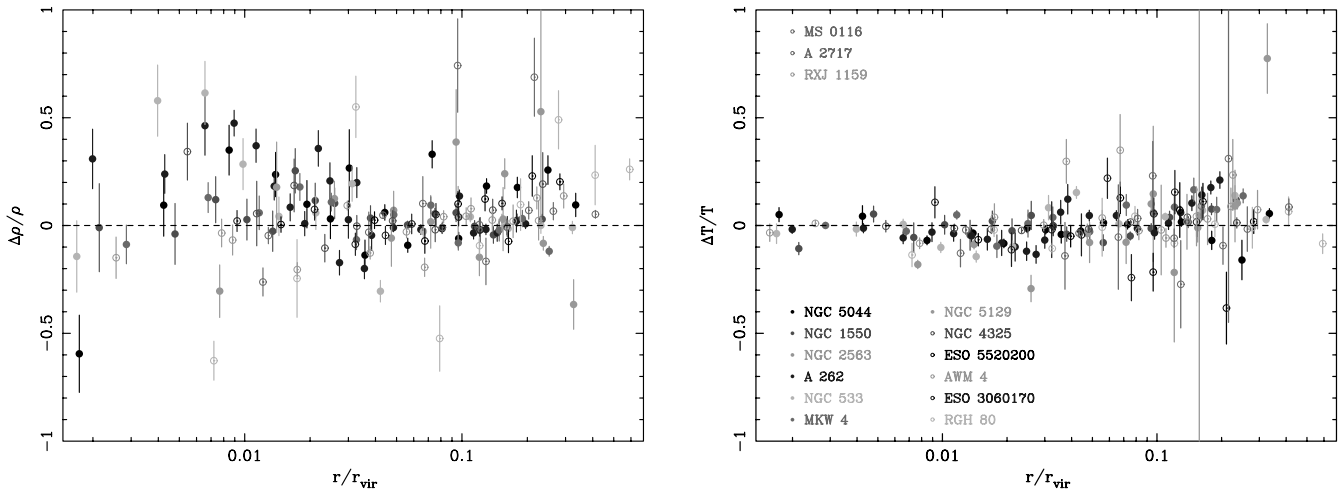

FIG. 7.—Comparison of 2D vs. 3D results: $(\rho_{2D} - \rho_{3D})/\rho_{3D}$ (*left*) and $(T_{2D} - T_{3D})/T_{3D}$ (*right*). Symbols used for the various systems are the same in both plots, and they are listed on the plot in the right panel. [*See the electronic edition of the Journal for a color version of this figure.*]

533 we obtain $c_\Delta = 5.3 \pm 0.4$, $M_\Delta = (1.41 \pm 0.06) \times 10^{13}\ M_\odot$, and $M_{\star,\Delta} = (31.6 \pm 2.1) \times 10^{11}\ M_\odot$.

9.5. *Mass Derivation Method*

For each system we tried all three methods described in § 6. By using all the approaches, we have an estimate of the robustness of the inferred mass and virial quantities. We also include in this estimate the fact that different temperature and density profiles may be able to fit the same data adequately but give rise to different global halo parameters. To test this, we cycled through each of our adopted gas density and temperature profiles.

9.6. *X-Ray Asymmetries and Disturbances*

There are systems displaying low-level asymmetries (IC 1860), substructure (RGH 80), and AGN cavities (A262) or possible AGN-induced disturbances (NGC 5044). For the objects that have a mild degree of disturbance in the core we found that the results obtained excluding the disturbed regions agreed with those obtained over the entire radial range within the 1–2 σ errors. For A262 we excluded the inner 20 kpc to avoid (1) the cavities that affect the central 10 kpc and (2) the stellar mass component of the central galaxy. In this case fitting an NFW profile gives $c_\Delta = 2.4 \pm 0.3$ and $M_\Delta = (3.44 \pm 0.15) \times 10^{13}\ M_\odot$. For NGC 5044 we obtain $c_\Delta = 3.9 \pm 0.1$ and $M_\Delta = (1.83 \pm 0.04) \times 10^{13}\ M_\odot$ after excluding the central 5 kpc, where there is evidence of a disturbed morphology. We exclude the inner 30 kpc of RGH 80 and find $c_\Delta = 6.5 \pm 1.0$ and $M_\Delta = (1.78 \pm 0.08) \times 10^{13}\ M_\odot$. Finally, for IC 1860 we perform a sector analysis, extracting spectra and rederiving our mass profiles from suitably oriented semiannuli, as detailed in § 8. We found consistent results within their $\sim$2 σ errors. Therefore, we infer no systematic error associated with including the central, mildly disturbed regions in these systems.

9.7. *Radial Range and Extrapolation*

It is customary to extrapolate mass profiles out to the virial radius defined within an overdensity $\Delta \sim 100$–500. This facilitates a consistent comparison to theoretical studies that usually quote results in this radial range, corresponding to the entire virialized portion of the halo. X-ray studies of global scaling relations between mass, temperature, and luminosity also prefer to use such large virial radii to seek the tightest relations between these global quantities.

However, extrapolating the mass profiles can lead to systematic errors in $c_{\rm vir}$, $M_{\rm vir}$, and the gas mass fraction. Vikhlinin et al. (2006) argue that biased extrapolation of the gas density profiles is the main reason for the underestimate of gravitational masses and low normalizations of the *M-T* relations found with earlier X-ray telescopes (e.g., Nevalainen et al. 2000), using a β model fit for the gas density and a polytropic approximation for the temperature profile. Rasia et al. (2006) suggest that the same systematic error affects $c_{\rm vir}$, in the sense that a restricted radial range tends to return a higher $c_{\rm vir}$, in the context of the NFW profile, than the value derived using data extending out to the virial radius.

Our procedure for mitigating extrapolation bias assuming that the halo follows an NFW profile is as follows. We obtain the mass profile within an appropriate r_Δ corresponding to the outer radius of the X-ray data for each group. The values of c_Δ and M_Δ are extrapolated to $\Delta \approx 101$ assuming that the NFW profile applies, using the convenient approximation of Hu & Kravtsov (2003). We emphasize that we do not need to extrapolate the models for the gas density and temperature to obtain the extrapolated mass parameters in this manner. The most important requirement for self-consistent extrapolation is that the NFW scale radius be accurately measured using the available X-ray data at smaller radius. Since our principal approach for measuring the mass profile (parametric mass method; see § 6) guarantees a physical solution of the equation of hydrostatic equilibrium for an NFW DM halo, unlike the methods used by Vikhlinin et al. (2006) and Rasia et al. (2006), and our temperature profiles are modeled with a more sophisticated approach than the polytropic-β model estimate, we expect more reliable measurements of r_s.

The crucial factor for reliable measurement of r_s is that the true value of r_s lies well within the outer radius of the X-ray data. We illustrate this effect using those objects for which we obtained measurements out to $\Delta = 500$ (A2717, RGH 80, and RX J1159.8+5531). If we exclude the outer two data points of A2717, then the new outer data point corresponds to 320 kpc and $\Delta = 2276$. Fitting the X-ray data over this mass range gives a best-fitting value, $r_s = 338$ kpc, uncomfortably outside the new radial range of the data and larger than inferred using all of the data ($r_s = 233$ kpc). Extrapolating this profile to $\Delta = 500$ yields a larger mass and a smaller concentration than obtained for all of the data. Analogous results are obtained when performing this exercise for RGH 80. For RX J1159.8+5531 we exclude the outer data point so that the new outer radius is 289 kpc, corresponding to

$\Delta = 2318$. In contrast to A2717 and RGH 80, when fitting over this smaller radial range, we obtain a scale radius 131 ± 76 kpc, still well within the outer radius. The derived mass parameters are $c_{2500} = 2.2 \pm 0.6$ and $M_{2500} = (3.69 \pm 0.86) \times 10^{13}\ M_{\odot}$. Extrapolating these values to $\Delta = 500$, we obtain $c_{500} = 4.7 \pm 1.1$ and $M_{500} = (7.10 \pm 3.25) \times 10^{13}\ M_{\odot}$, in excellent agreement with the results obtained over the whole data range presented in Table 3.

This exercise suggests that measurements of c_{Δ} and M_{Δ} should be reliable provided that the NFW scale radius lies well within the outermost radius covered by the data, as is the case for all the objects in our sample. Agreement with the optical determination of the scale radius for the two objects in common with Rines & Diaferio (2006) adds further strength to the results (see § 8).

Unfortunately, extrapolation of the gas mass and gas fraction is less reliable. If we extrapolate our models out to a virial radius corresponding to $\Delta \sim 101$, we obtain gas fractions consistent with the cosmic value in 12 of 16 cases. In 4 cases the extrapolated gas fractions exceed the cosmic value derived by *WMAP*, suggesting a problem with the extrapolation. All these systems possess a flat slope of the gas density profile ($\beta < 0.5$) at the edge of the data range. This type of behavior has been noted previously by simulations and simple analytic models that pointed out how the β model overestimates gas mass (and underestimates gravitational masses based on β model fits) because it returns a biased low β due to the restricted range of radii where the fit is performed (Navarro et al. 1995; Bartelmann & Steinmetz 1996; Borgani et al. 2004; Komatsu & Seljak 2001). Indeed, Vikhlinin et al. (2006) find evidence for a steepening of the gas density slope with radius in clusters.

9.8. *The Stellar Mass Profile of the Central Galaxy*

To account for the stellar component, we adopted a de Vaucouleurs model with effective radius being fixed to that determined by 2MASS. The derived stellar mass is most sensitive to the effective radius. The difference in effective radii measured in different optical bands, as evident in Table 2, is mainly due to the use of different fitting ranges/sensitivity (e.g., Fisher et al. 1995) and to a radial color gradient, reflecting gradients in the metallicity or age of the stellar population (e.g., Pahre 1999). Although the true stellar mass is more reliably determined from *K*-band data, we investigated the sensitivity of our parameters, in particular the value for $M_{\star}/L$, to the choice of r_e, by replacing the *K*-band r_e for each galaxy with the larger *B*-band value, listed in the Third Reference Catalog of Bright Galaxies (RC3; de Vaucouleurs et al. 1991). The stellar mass, and consequently $M_{\star}/L$, increases systematically, with the only exception being NGC 533, when using the larger *B*-band effective radius. But, importantly, the concentration and mass are not affected, showing that the main conclusions of our paper regarding these two quantities are not sensitively dependent on the adopted stellar template.

We studied the possible contribution to the stellar mass of noncentral galaxies within r_s using known member galaxies with 2MASS photometry as listed in NED. For most of the objects they contribute no more than 10% of the total light. This is consistent with the more general result of Lin & Mohr (2004), who showed that the ratio of brightest cluster galaxies (BCGs) to total galaxy light decreases with increasing cluster mass, indicating that 30%–50% of the total light in galaxies is in the BCGs for group-scale systems ($10^{13}\ M_{\odot} < M_{200} < 10^{14}\ M_{\odot}$). Notable exceptions are in fact the most massive objects in our sample: A262 has a 77% and AWM 4 a 39% additional contribution from noncentral galaxies within r_s.

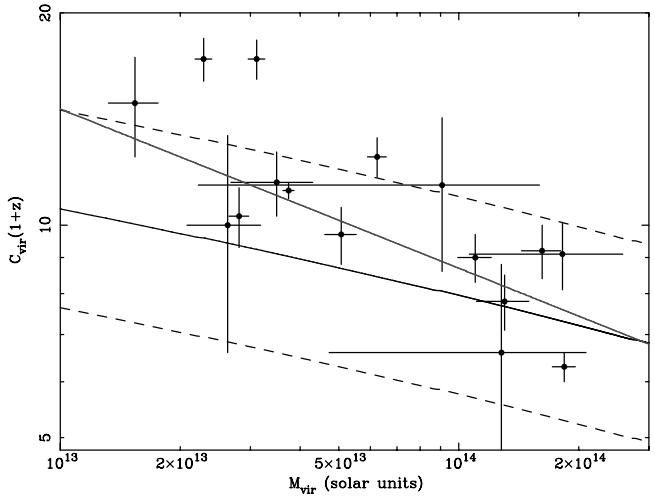

FIG. 8.— Concentration parameters $c_{\rm vir}$ (multiplied by $1 + z$) vs. the group mass $M_{\rm vir}$. The black solid line represents the median $c_{\rm vir}(M_{\rm vir})$ relation and the outer dotted lines the 1 σ scatter ($\Delta \log c_{\rm vir} = 0.14$) calculated according to the model of Bullock et al. (2001) with parameters $F = 0.001$ and $K = 3.12$ and for a concordance model with $\sigma_8 = 0.9$. The gray solid line represents the best-fitting power-law relation discussed in the text. [*See the electronic edition of the Journal for a color version of this figure.*]

10. DISCUSSION

10.1. $c_{\rm vir}$-$M_{\rm vir}$ *Relation*

In Figure 8 we plot the $c_{\rm vir}$-$M_{\rm vir}$ relation fits to the *XMM-Newton* and *Chandra* data ($\Delta \approx 101$; see Table 7 below). To obtain an empirical description of the relation, we fitted a simple power-law model following the approach described in Buote et al. (2007). That is, we fitted the data with a linear relation of the form $\log (1 + z)c_{\rm vir} = \alpha \log M_{\rm vir} + b$ using the BCES estimator of Akritas & Bershady (1996) with bootstrap resampling. We obtain $\alpha = -0.226 \pm 0.076$, implying that the concentration decreases with increasing mass at the 3 σ level. The previous studies of clusters ($>10^{14}\ M_{\odot}$) with *Chandra* and *XMM-Newton* found $\alpha \approx 0$, very consistent with a constant $c_{\rm vir}$-$M_{\rm vir}$ relation (Pointecouteau et al. 2005; Vikhlinin et al. 2006). Therefore, it is the lower mass range, 10^{13}–$10^{14}\ M_{\odot}$, appropriate for groups that provides crucial evidence that $c_{\rm vir}$ decreases with increasing $M_{\rm vir}$ as expected in CDM models (e.g., Bullock et al. 2001).

The best-fitting power-law model is plotted in Figure 5 along with the theoretical prediction of the ΛCDM obtained using the model of Bullock et al. (2001) with parameters ($F = 0.001, K = 3.12$) intended to represent halos up to masses $\sim 10^{14}\ M_{\odot}$. Also shown is the predicted 1 σ intrinsic scatter for the ΛCDM model. For $M \gtrsim 4 \times 10^{13}\ M_{\odot}$ the ΛCDM model is a good representation of the X-ray data. For lower masses, the observed $c_{\rm vir}$-$M_{\rm vir}$ appear to exceed the prediction. Allowing for a ≈10% increase in the concentrations predicted by the ΛCDM model for the most relaxed, early forming halos (Jing 2000; Wechsler et al. 2002; Macciò et al. 2007) helps to bring the model into better agreement with the observations.

We infer an intrinsic scatter, 0.03 ± 0.02, in $\log_{10}(1 + z)c$ for the empirical power-law relation (see Buote et al. 2007), which is considerably less than the value of ≈0.14 obtained for ΛCDM halos (Jing 2000; Wechsler et al. 2002; Macciò et al. 2007). For the most relaxed, early forming halos ΛCDM simulations typically find a smaller scatter ∼0.10 (Wechsler et al. 2002; Macciò et al. 2007), although the most relaxed halos studied by Jing (2000) have a scatter of 0.07 (after converting between ln and $\log_{10}$ with a factor of 2.3). The small scatter we have measured about the

power-law relation only agrees with CDM simulations if these halos are the most relaxed, early forming systems.

The data-model comparison has been made for a ΛCDM model with parameters obtained from the first-year *WMAP* results (Spergel et al. 2003), in particular with $\Omega_m = 0.3$ and $\sigma_8 = 0.9$. With the lower values favored by the three-year data release of *WMAP* (Spergel et al. 2007) the predicted concentrations are lower (see, e.g., discussion in Macciò et al. 2007). The implications are discussed in Buote et al. (2007).

10.2. *The Detection of Central Stellar Mass*

A good fit of the NFW profile to the total gravitating matter of relaxed, $T > 3$ keV, massive clusters, without any significant deviation arising from the central stellar mass, appears to be a common feature of X-ray studies (Pointecouteau et al. 2005; Vikhlinin et al. 2006; Zappacosta et al. 2006). On the contrary, relaxed bright elliptical galaxies always require a dominant contribution of stellar mass (Humphrey et al. 2006). The intermediate mass range explored here shows a mixed behavior: some low-mass, group-scale objects and three poor clusters (AWM 4, RX J1159, and Abell 262) do show evidence of stellar mass, while there are examples of objects whose gravitating mass profile is described by just NFW. (Note that RX J1159, A262, and MKW 4 were also shown to have an excess core mass profile above that indicated by NFW in the analysis of Vikhlinin et al. 2006.)

An important issue emerging in the analysis is how well the two key components, the stellar component associated with the central galaxy and the DM, are sampled by the X-ray data. It is expected that the stellar component is most relevant within the inner 10–20 kpc while the DM should dominate the mass budget elsewhere. To reveal and measure adequately the stellar mass, enough density and temperature data points are required in the inner ∼20 kpc, depending as well on the amount of stellar mass present (implied by L_K). The omission of the stellar component in the mass modeling, proposed as a possible source of abnormally high c (Mamon & Łokas 2005), is certainly a factor for relatively nearby objects with data densely sampling the inner dominated stellar core but not extending to large radii, as for the objects analyzed with *Chandra* data in Humphrey et al. (2006). The effect is less pronounced in the objects analyzed in this sample, where the data extend to large enough radii, but with comparatively less density of data points in the inner 20 kpc, in particular for objects with only *XMM-Newton* observations. The presence of data at large radii prevents us from obtaining large values of $c_{\rm vir}$ ($\geq$30) when fitting the wrong NFW model to objects that require stellar mass.

For the objects that require stellar mass and have 2–3 data bins in the inner 20 kpc (NGC 1550, A262, NGC 533, MKW 4) the derived stellar M/L ratios are consistent with the range of values found in our analysis of a sample of elliptical galaxies (Humphrey et al. 2006): the (unweighted) mean M/L ratio of these four objects is 0.57 ± 0.21, which is consistent within 1 σ with 0.76 ± 0.24, the mean stellar M/L ratio of the objects in Humphrey et al. (2006), although a 25% difference is present. This result reinforces the relevance of the sampling of the inner region: on average the objects in Humphrey et al. (2006) have ∼7 data bins in the inner 20 kpc, allowing a more accurate measurement of the stellar mass. The measures for objects with low-resolution *XMM-Newton* observations are likely biased low, as we determined for objects with both *XMM-Newton* and *Chandra* observations.

For a single-burst stellar population (SSP) with age ranging from 9 to 13 Gyr and metallicity ranging from 0.5 to 2 solar, the K-band stellar mass-to-light ratio is expected to take values in the range 0.86–1.16 for a Kroupa IMF (Kroupa 2001) and 1.28–1.49 for a Salpeter IMF (Salpeter 1955). (We have used linearly interpolated synthetic $M_\star/L_K$ values based on the stellar population models of Maraston [1998] from updated model grids made available by the author[7] and converting from their definition of $M_{K_s,\odot} = 3.41$.) The measurements are, therefore, in reasonable agreement with the SSP models assuming a Kroupa IMF, given the uncertainties in both the data and models.

Clearly the X-ray determination of the stellar mass contribution in these objects can benefit from deeper observations, and the systematics involved in the modeling of the stellar profile, like the value of the effective radius, impacts the results considerably. However, the excellent agreement between the gravitating mass-to-light ratio at the effective radius obtained from X-rays and globular cluster kinematics for the elliptical galaxy NGC 4649 by Bridges et al. (2006) provides strong support for the reliability of the stellar mass-to-light ratio determined from X-rays in that system.

Stellar mass has not been detected for NGC 5044, RGH 80, and NGC 4325, systems that do have *Chandra* data, allowing a reasonable sampling of the inner core. Better *Chandra* data would be required in the core of NGC 5044 to measure possible localized disturbances due to AGN activity, which can be a likely source of systematics in the mass measurement in the inner 10–20 kpc. Hints of disturbances (cavities) due to AGN activity have also been detected in NGC 4325 (Russell et al. 2007). There is evidence from the optical and the *Chandra* X-ray image that the core of RGH 80 may not be completely relaxed. Therefore, localized departures from hydrostatic equilibrium in the core of these systems are likely explanations for the failure to detect stellar mass.

If we allowed the DM profile to be modified by adiabatic contraction, we obtained substantially smaller $M_\star/L_K$ for our data, which are more discrepant with SSP models, casting doubt on the importance of the adiabatic contraction process. We obtained similar results in our study on elliptical galaxies (Humphrey et al. 2006 and discussion therein of other observational results). Recently Gustafsson et al. (2006) proposed that also the details of the feedback and its effect on the concentration of the baryons are an important ingredient for the determination of the final contracted DM halo.

We tested the sensitivity of the measured concentrations and gravitational masses to the stellar template by substituting the effective radius of the de Vaucouleurs model derived by 2MASS with the larger value listed in RC3. By doing that, the stellar mass-to-light ratio can increase up to 80%, but the concentration and gravitational mass are not affected as dramatically (see § 9.8). The latter measurements seem therefore robust to the assessment of the precise best-fit model for the light profile of BCGs and the precise measurement of their size (a task that requires particular care [e.g., Bernardi et al. 2007; Seigar et al. 2007] and that is beyond the scope of this paper).

10.3. *Gas Fractions*

In Figure 9 we plot the gas fractions for the objects in our sample, calculated within a radius corresponding to an overdensity of $\Delta = 2500$ and 1250, as a function of virial mass. No significant trend of gas fraction with mass is present, while there is significant object-to-object scatter: the average values of the gas fractions are $f_{\rm gas,2500} = 0.053 \pm 0.012$ and $f_{\rm gas,1250} = 0.069 \pm 0.014$. The mean value of $f_{\rm gas,2500}$ obtained for the groups in our sample is significantly smaller than that obtained from the hot, massive clusters ($T > 5$ keV) studied by Allen et al. (2004),

[7] See http://www-astro.physics.ox.ac.uk/~maraston/Claudia%27s_Stellar_Population_Models.html.

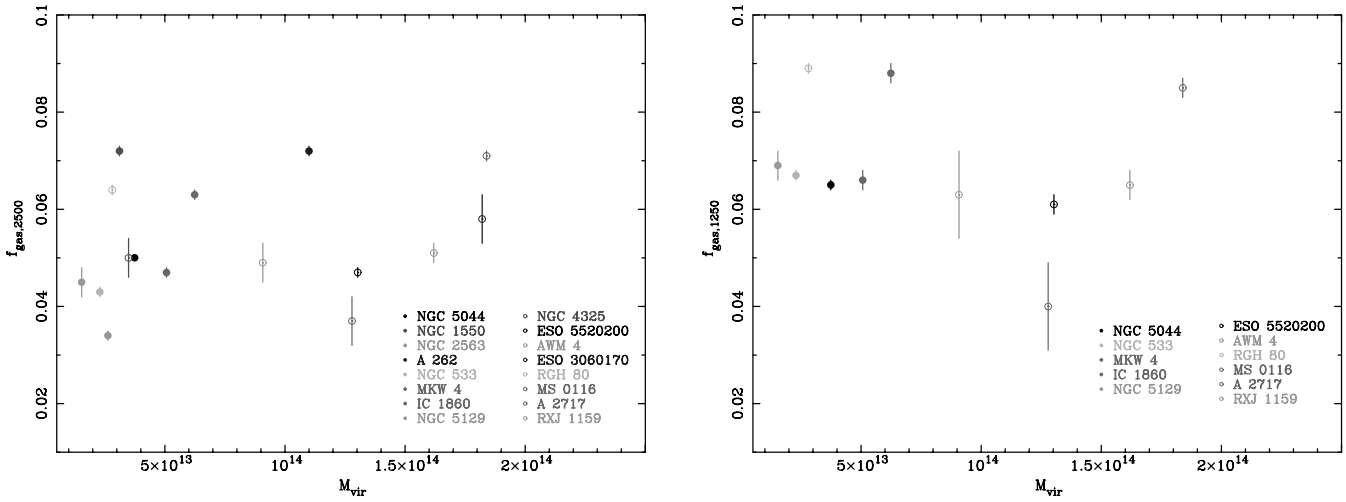

FIG. 9.—Observed gas fractions within r_{2500} (*left*) and within r_{1250} (*right*) as a function of the virial mass. Errors bars on the virial mass have not been shown for clarity of the plot. [*See the electronic edition of the Journal for a color version of this figure*.]

$f_{\rm gas,2500} = 0.118 \pm 0.016$, and Vikhlinin et al. (2006), $f_{\rm gas,2500} = 0.092 \pm 0.004$. (Note that we quote the mean and standard deviation, not the Gaussian error-weighted mean and error, because of the possibility of non-Gaussian contributions to the gas fraction distributions, such as intrinsic scatter caused by scale-dependent feedback processes.) The fractional error obtained for our groups, $\sigma_f/f = 0.2$, exceeds the values of 0.14 and 0.04 for, respectively, the clusters of Allen et al. (2004) and Vikhlinin et al. (2006). Therefore, there is a clear mass dependence on the gas fraction (mean and fractional scatter), not surprising given that the expected feedback energy injection by AGNs should be more severe at the group scale.

The extrapolation of gas quantities outside the radial range of the data is dangerous (see § 9.7). However, for most of the groups in our sample, we find that the extrapolated gas fraction, coupled with the estimate of the stellar mass, yields global baryon fractions consistent with the universal value, i.e., consistent with the notion that X-ray–bright groups are baryonically closed (Mathews et al. 2005). This result suggests that for the objects in our sample for which the slope of the gas density profile is not too flat ($\beta \gtrsim 0.5$), the extrapolation of the gas fraction is also fairly reliable. Data at large radii are much needed to further explore this issue.

10.4. *Temperature Profiles*

The temperature profiles of our groups (Figs. 3, 4, 5, and 6) exhibit the same behavior characteristic of cool core clusters (Markevitch et al. 1998; De Grandi & Molendi 2002; Piffaretti et al. 2005; Vikhlinin et al. 2005; Pratt et al. 2007); i.e., the temperature profile rises outward from the center, reaches a maximum, and then falls at large radius. To examine the self-similarity of the profiles, we first rescaled them in terms of the virial radii. Then we normalized each profile according to the gas mass–weighted temperature ($T_{\rm gmw}$) computed between $0.1r_{\rm vir}$ and $0.3r_{\rm vir}$ using the temperature and gas density models we derived for each system (gas mass weighting should be more closely related to the gravitational potential than emission weighting; e.g., Mathiesen & Evrard 2001). We find that the scaled temperature profiles are approximately self-similar for $r > 0.15r_{\rm vir}$, but there is a large amount of scatter at smaller radii ($r < 0.1r_{\rm vir}$). This behavior is qualitatively similar to that found in clusters by Vikhlinin et al. (2006) although the large scatter in the cores suggests that feedback (AGN) processes have had a more dramatic impact at the group scale, e.g., the striking isothermal core of AWM 4.

Unlike the rise-then-fall temperature profiles observed for relaxed, cool core groups and clusters with $M \gtrsim 10^{13}\,M_\odot$, the three galaxy scale systems ($M < 10^{13}\,M_\odot$) we studied in Humphrey et al. (2006) all have temperature profiles that decrease monotonically with increasing radius. Hence, the temperature profiles observed in our present study provide further support for the suggestion we made in Humphrey et al. (2006) that $\approx 10^{13}\,M_\odot$ represents the mass scale demarcating the transition between (field) galaxies and groups. The dramatic change in M/L ratios observed at this mass scale from optical and lensing studies (Parker et al. 2005 and references therein) gives additional evidence that $\approx 10^{13}\,M_\odot$ is a special mass scale.

10.5. *Reliability of X-Ray Mass and Concentration Estimates*

Key sources of systematic errors in the X-ray determination of mass and concentration parameters discussed in the literature can be listed as follows: the applicability of hydrostatic equilibrium, a correct interpretation of the temperature measured by X-ray satellites (i.e., spectroscopic vs. emission weighted; e.g., Mazzotta et al. 2004), and the restricted radial range over which the mass is inferred.

The results presented in this paper show how mass constraints for X-ray–bright groups/poor clusters derived from good-quality *XMM-Newton* and *Chandra* observations can be of the same quality as obtained for hot, massive clusters. The objects in our sample have been chosen following similar criteria for selecting relaxed clusters for mass studies (e.g., Pointecouteau et al. 2005; Vikhlinin et al. 2006). Indeed, our results show strong support for a scenario where hydrostatic equilibrium is an excellent approximation. The mass profiles inferred from density and temperature profiles are in good agreement with the predicted quasi-universal NFW profile, and the concentration parameters are as expected (i.e., for ΛCDM) for the masses of these objects. The observed trend toward more concentrated halos, as expected from numerical simulations for relaxed halos that have not experienced a recent major merger, provides further verification of our selection criteria. The fits based on the equation of hydrostatic equilibrium were able to model complicated temperature and density profiles (assuming a simple NFW DM halo and central stellar component) that would be surprising if the gas is significantly out of hydrostatic equilibrium.

The estimate of the real temperature from the projected X-ray temperature has been discussed as a source of systematic error in

X-ray mass estimates. If a spectrum contains several components with different T and metallicity, the "spectroscopic temperature" derived from a single-temperature fit is biased toward lower temperature components (Mazzotta et al. 2004; Vikhlinin et al. 2006). But the particular temperature range of 1–3 keV explored in this paper is sensitive to the presence of complex thermal structure because the Fe L-shell line complex is very prominent in the spectrum and able to discern different temperature components (Buote 2000a, 2000c; Böhringer et al. 2002). If a spectrum contains components with different temperatures, the residuals have a characteristic shape, originally noted in *ASCA* large-beam spectra as the "Fe bias" because the Fe abundance derived from such a spectrum is biased low (Buote 2000c). Although the Fe abundance is biased low in such cases, the inferred average temperature is not biased for $\sim$1 keV systems, as shown in this paper and in the Appendix of Buote (2000c). (Note that such an underestimate in the Fe abundance will lead to an overestimate of the gas density. But if the bandpass extends down at least to $\approx$0.5 keV, as it does for the ACIS and EPIC data, the Fe bias is reduced significantly [Buote 2000b]. Further reduction in the Fe bias from previous large-beam *ASCA* studies results from using much thinner annuli, especially in the core regions exhibiting the steepest temperature gradients where the bias would be largest. Considering that the Fe-L line emission contributes less than the bremsstrahlung over the ACIS and EPIC bandpasses and that the gas density varies as the square root of the emissivity, the reduced Fe bias leads to a minor overestimate of the gas density that is less than the statistical error and other systematic errors considered in this paper.)

What remains to be determined is whether the gas is truly single phase. The use of annuli with the smallest possible radial width, allowed by the superb *Chandra* spatial resolution, is crucial to ensure that the multiphase appearance is not simply due to a single-phase temperature gradient. The multiphase appearance of *XMM-Newton* spectra extracted in the core of groups like NGC 533 (Kaastra et al. 2004) and RGH 80 (Xue et al. 2004) is caused mainly by this reason. This possible error, i.e., assuming that the gas is single phase when it is actually multiphase, only could affect the innermost regions where the temperature gradient is most pronounced. Therefore, this possible source of systematic error in some systems can be relevant only for obtaining the most precise measurement of the stellar mass, but it is unimportant for determinations of the halo mass and concentration.

For the objects in our sample the scale radius is well within the radial range covered by the data. Therefore, a restricted radial range, even for objects for which we reach an overdensity of 2500, should not be an important source of systematic error in the measurement of concentration parameters, as we showed in § 9.7.

We also found that our results are not sensitive to mild disturbances related to the presence of a central AGN or to a not fully relaxed dynamical state (§ 9.6). The derived concentrations and masses are also quite insensitive to errors in the shape of the stellar mass profile of the central galaxy (§ 9.8).

It is still very interesting and desirable to obtain data at larger radii with offset observations performed by the current generation of X-ray observatories, in particular *XMM-Newton*, rather than still rely on *ROSAT*, in particular to measure gas masses and gas fraction (and to further constrain the total mass). Molendi (2004), addressing the issue of our ignorance of the outer regions of hot massive clusters, pointed out how a combination of reduction of particle background to lower levels compared to the cosmic background and the use of a differential measure, to improve the knowledge of the actual background in the observation, is key to a successful measure of the very low surface brightness regime at large radii. The discussion in Molendi (2004) is focused in particular on measuring the exponential cutoff of the bremsstrahlung spectrum of a cluster with $T > 3$ keV. For the particular case of groups/poor clusters, where instead the temperature is determined by the Fe L shell, the clear separation of the source component (at least over the radial range where the temperature is not declining at values comparable to the temperature of the soft Galactic background) from all the other background components is an effective way of making a differential measure because we know both the source and the background. The use of the improved *XMM-Newton* capabilities in terms of collecting area and spectral resolution with respect to *ROSAT* will also lift the likely important metallicity-density degeneracy (which is even more important at large radii, being the group emission due to line emission). Furthermore, the planned future X-ray observatories, like *Xeus* and *Constellation-X*, will have a smaller field of view, and the mapping of the outer regions of nearby systems will be even more demanding in terms of observing time.

11. SUMMARY

Using *Chandra* and *XMM-Newton* data, we have obtained detailed density, temperature, and mass profiles of 16 groups/poor clusters that were selected to be highly relaxed systems with the best available data. We summarize as follows:

1. The mass profiles were well described by a two-component model: an NFW model for the DM and a de Vaucouleurs stellar mass model for eight objects. For objects without adequate sampling in the inner 20 kpc and for NGC 5044, NGC 4325, and RGH 80 a pure NFW model was a good fit of the data. A possible explanation for the failure to detect stellar mass in NGC 5044 and NGC 4325 is localized disturbance by AGN activity and for RGH 80 incomplete relaxation in the core. For objects with evidence of stellar mass, the stellar mass-to-light ratio in the K band was found to be in approximate agreement with simple stellar population synthesis models, assuming a Kroupa IMF.

2. Adopting more complicated models, like introducing adiabatic contraction or the recently proposed N04 DM profile, did not improve the fits. With the available data, AC produces too low stellar mass-to-light ratios and N04 has too high inverse Sérsic indexes.

3. The measured $c_{\rm vir}$-$M_{\rm vir}$ relation agrees with the predictions of ΛCDM with $\sigma_8 = 0.9$ and $\Omega_m = 0.3$. In particular, in the mass range of our group sample the expected decrease of $c_{\rm vir}$ with $M_{\rm vir}$ has been detected for the first time. There is a trend, common to all X-ray observations, toward more concentrated halos, which can be understood in terms of a selection bias, already explored in numerical simulations, toward relaxed, earlier forming systems.

4. The gas fraction measured at an overdensity of 2500 is lower than the one measured for hot, massive clusters and has higher scatter, as expected if feedback has played a more severe role at this mass scale. However, the gas fractions increase with radius, and for objects with data extending to large radii, these objects are consistent with being baryonically closed. However, the gas fractions increase with radius, and for objects with data extending to large radii, these objects are consistent with being baryonically closed.

5. When rescaling the radial temperature profiles in terms of $r_{\rm vir}$ and also the gas mass–weighted temperature (evaluated over $0.1r_{\rm vir}$–$0.3r_{\rm vir}$), we find that the scaled profiles show a fair amount of similarity beyond $0.15r_{\rm vir}$. In the core ($r < 0.10r_{\rm vir}$) the scaled profiles have a large amount of scatter, again suggesting the important role of feedback in these groups.

6. We tested the robustness of our results, performing a careful analysis of possible systematic errors, like background subtraction, departures from hydrostatic equilibrium, and deprojection method, and found none of them to seriously affect our analysis and results.

We thank the referee for helpful suggestions that improved the presentation of the paper. We would like to thank Oleg Gnedin for making available his adiabatic compression code. We thank A. De Luca, S. Ettori, A. Kravtsov, G. Mamon, P. Mazzotta, S. Molendi, and A. Vikhlinin for interesting discussions. This work is based on observations obtained with *XMM-Newton*, an ESA science mission with instruments and contributions directly funded by ESA member states and the USA (NASA). This research has made use of data obtained from the High Energy Astrophysics Science Archive Research Center (HEASARC), provided by NASA's Goddard Space Flight Center. This research has also made use of the NASA/IPAC Extragalactic Database (NED), which is operated by the Jet Propulsion Laboratory, California Institute of Technology, under contract with NASA. In addition, this work also made use of the HyperLeda database. D. A. B. and F. G. gratefully acknowledge partial support from NASA grant NAG5-13059, issued through the Office of Space Science Astrophysics Data Program. Partial support for this work was also provided by NASA through *Chandra* awards GO4-5139X and GO6-7118X issued by the *Chandra* X-Ray Center, which is operated by the Smithsonian Astrophysical Observatory for and on behalf of NASA under contract NAS8-03060. We also are grateful for partial support from NASA-XMM grants NAG5-13643, NAG5-13693, and NNG05GL02G.

APPENDIX A

MASSES AND CONCENTRATION PARAMETERS AT DIFFERENT OVERDENSITIES

Following Arnaud et al. (2005) and Vikhlinin et al. (2006), we quote in Table 7 mass, concentration parameters, and characteristic radii at different overdensities. The virial quantities obtained in our fits have been rescaled to the often-used overdensity levels of $\Delta = 500$, 200, and $\Delta_{\rm vir}$ listed in Table 1 using the fitting formula of Hu & Kravtsov (2003), which for $c < 20$ is accurate to 0.3%.

APPENDIX B

RELATING X-RAY OBSERVATIONS TO SPHERICAL MODELS OF CORONAL GAS WITH VARIABLE PLASMA EMISSIVITY

We relate the spherical models of density (ρ_g) and temperature (T) of the hot gas in elliptical galaxies, galaxy groups, and clusters (§ 6) to the parameters obtained from conventional spectral fitting of X-ray data, such as from *Chandra* and *XMM-Newton*. Since much of the relevant material is scattered throughout the literature spanning over at least 30 years, this appendix provides an opportunity to give a self-contained, up-to-date presentation. Our treatment fully accounts for radial variations of the plasma emissivity that are often neglected, especially when inferring the gas density. We follow the standard procedure where emission from coronal plasma characterized by a single temperature (1T) is fitted to the X-ray spectrum extracted from a circular annulus (2D) or, if the data have been deprojected, a spherical shell (3D). The density and temperature (and abundance) parameters obtained from such a 1T fit are compared to the emission-weighted (and projected if 2D) spherical models of ρ_g and T (and abundances). It is assumed that the annuli are chosen to be sufficiently wide so that the detector PSF may be neglected. We discuss additional weighting by detector responses at the end of this section.

For any spectral quantity, such as luminosity (ergs s^{-1}), that results from integrating between photon energy E_1 and energy E_2, we use the notation

$$L(\Delta E) \equiv \int_{E_1}^{E_2} \frac{dL}{dE}\, dE \tag{B1}$$

TABLE 7
Results for the NFW Profile at Different Overdensities

Group (kpc)	$c_{\rm vir}$	$r_{\rm vir}$ (kpc)	$M_{\rm vir}$ ($10^{13}\ M_\odot$)	c_{500}	r_{500} (kpc)	M_{500} ($10^{13}\ M_\odot$)	c_{200}	r_{200} (kpc)	M_{200} ($10^{13}\ M_\odot$)
NGC 5044	11.1 ± 0.3	860 ± 9	3.74 ± 0.12	5.7 ± 0.1	443 ± 4	2.51 ± 0.07	8.4 ± 0.2	653 ± 7	3.21 ± 0.10
NGC 1550	17.0 ± 1.1	811 ± 13	3.11 ± 0.15	9.0 ± 0.6	428 ± 6	2.24 ± 0.09	13.0 ± 0.9	621 ± 9	2.73 ± 0.12
NGC 2563	9.9 ± 3.4	762 ± 55	2.63 ± 0.55	5.1 ± 1.9	390 ± 22	1.72 ± 0.28	7.5 ± 2.6	577 ± 39	2.24 ± 0.43
A262	8.9 ± 0.7	1232 ± 38	11.00 ± 1.06	4.5 ± 0.4	624 ± 15	7.02 ± 0.52	6.7 ± 0.5	930 ± 27	9.29 ± 0.82
NGC 533	16.9 ± 1.2	727 ± 12	2.29 ± 0.11	9.0 ± 0.7	385 ± 5	1.65 ± 0.06	13.0 ± 0.9	559 ± 8	2.02 ± 0.09
MKW 4	12.3 ± 0.8	1012 ± 18	6.24 ± 0.34	6.4 ± 0.5	527 ± 8	4.27 ± 0.18	9.4 ± 0.7	773 ± 13	5.40 ± 0.27
IC 1860	9.5 ± 0.9	946 ± 29	5.07 ± 0.46	4.9 ± 0.5	484 ± 11	3.31 ± 0.23	7.2 ± 0.7	718 ± 20	4.30 ± 0.36
NGC 5129	14.6 ± 2.4	636 ± 29	1.54 ± 0.22	7.7 ± 1.3	335 ± 12	1.09 ± 0.12	11.2 ± 1.9	488 ± 21	1.35 ± 0.18
NGC 4325	11.2 ± 1.2	833 ± 57	3.49 ± 0.81	5.8 ± 0.7	432 ± 25	2.36 ± 0.45	8.6 ± 1.0	635 ± 41	3.01 ± 0.65
ESO 5520200	7.6 ± 0.7	1288 ± 61	13.03 ± 1.95	3.9 ± 0.4	650 ± 24	8.05 ± 0.94	5.8 ± 0.6	976 ± 43	10.90 ± 1.51
AWM 4	8.9 ± 0.8	1384 ± 53	16.19 ± 1.82	4.6 ± 0.5	708 ± 23	10.44 ± 0.99	6.8 ± 0.6	1054 ± 38	13.75 ± 1.46
ESO 3060170	8.8 ± 1.0	1436 ± 141	18.21 ± 7.58	4.5 ± 0.6	733 ± 59	11.67 ± 3.72	6.7 ± 0.8	1093 ± 100	15.44 ± 5.86
RGH 80	9.9 ± 1.0	771 ± 15	2.81 ± 0.16	5.1 ± 0.5	398 ± 5	1.86 ± 0.07	7.6 ± 0.8	588 ± 10	2.41 ± 0.12
MS 0116.3−0115	6.3 ± 2.1	1272 ± 220	12.79 ± 8.06	3.1 ± 1.2	634 ± 85	7.54 ± 3.41	4.8 ± 1.7	962 ± 153	10.55 ± 5.92
A2717	6.0 ± 0.3	1432 ± 31	18.39 ± 1.22	3.0 ± 0.2	710 ± 12	10.68 ± 0.52	4.6 ± 0.3	1082 ± 21	15.10 ± 0.89
RX J1159.8+5531	10.6 ± 2.6	1110 ± 177	9.08 ± 6.86	5.6 ± 1.5	585 ± 73	6.16 ± 3.29	8.3 ± 2.1	861 ± 127	7.87 ± 5.33

to represent the bandpass integration. For a coronal plasma emitting within a volume V_i at a temperature T_i with chemical abundances $Z_{\mathrm{Fe},i}$, $Z_{\mathrm{O},i}$, $Z_{\mathrm{Si},i}$, etc., the luminosity is given in XSPEC by

$$L(\Delta E)_i = 4\pi[D_A(1+z)]^2 \mathrm{norm}_i \Lambda^{\mathrm{XS}}(T_i,\, Z_i;\, \Delta E), \tag{B2}$$

where we have used the symbol Z_i to represent all the abundances, z is the redshift, D_A is the angular diameter distance (cm), and Λ^{XS} is the plasma emissivity (ergs s^{-1} cm^3) corresponding to the XSPEC implementation of the relevant coronal plasma code (e.g., APEC, MEKAL). To give a precise definition[8] of norm_i that accounts for spatial variations of the temperature and abundances within V_i, we refer to the volume emissivity (ergs s^{-1} cm^{-3}) of a coronal plasma,

$$\epsilon(\boldsymbol{x};\, \Delta E) = n_e(\boldsymbol{x}) n_{\mathrm{H}}(\boldsymbol{x}) \Lambda(T(\boldsymbol{x}),\, Z(\boldsymbol{x});\, \Delta E), \tag{B3}$$

where, e.g., $T(\boldsymbol{x}) \equiv T(x, y, z)$, and the plasma emissivity in XSPEC is related to the conventional definition[9] by $\Lambda^{\mathrm{XS}} \equiv 10^{14}\Lambda$. It is convenient to work in terms of the volume mass density of the gas, $\rho_g(\boldsymbol{x})$, rather than the volume number densities, $n_e(\boldsymbol{x})$ and $n_{\mathrm{H}}(\boldsymbol{x})$, separately. To a very good approximation, for this calculation one may assume a fully ionized gas of pure H and He, in which case

$$n_e = \frac{2+\mu}{5\mu}\frac{\rho_g}{m_u}, \qquad n_{\mathrm{H}} = \frac{4-3\mu}{5\mu}\frac{\rho_g}{m_u}, \tag{B4}$$

where μ is the mean atomic weight of the gas and m_u is the atomic mass unit. (Note that using $\mu = 0.62$ corresponding to the solar He abundance leads to $n_e = 1.22 n_{\mathrm{H}}$.) By setting equation (B2) equal to the luminosity obtained by integrating equation (B3) over the volume V_i and solving for norm_i, one finds

$$\mathrm{norm}_i = \left\{\frac{10^{-14}}{4\pi[D_A(1+z)]^2}\,\frac{(2+\mu)(4-3\mu)}{(5\mu)^2 m_u^2}\right\}\frac{1}{\Lambda^{\mathrm{XS}}(T_i,\, Z_i;\, \Delta E)}\int_{V_i}\rho_g^2(\boldsymbol{x})\Lambda^{\mathrm{XS}}(T(\boldsymbol{x}),\, Z(\boldsymbol{x});\, \Delta E)\, d^3x, \tag{B5}$$

where $\mathrm{norm}_i \propto \int \rho_g^2\, d^3x$ if Λ^{XS} is constant over the volume V_i. If Λ^{XS} varies over the volume, then the parameters T_i and Z_i obtained from fitting a 1T coronal plasma model to the spectrum with multiple temperatures and abundances will reflect average quantities weighted by the emission profile within the volume and the detector response. We defer treatment of the detector response to the end of this section and focus now on the deprojection and projection of emission-weighted spherical quantities.

Deprojection analysis.—If the spectra are deprojected so that the norm_i values refer to spherical shells, then equation (B5) can be immediately recast in terms of the weighted square of the gas density,

$$\left\langle \rho_g^2 \right\rangle_i \equiv \left\{\frac{4\pi[D_A(1+z)]^2}{10^{-14}}\,\frac{(5\mu)^2 m_u^2}{(2+\mu)(4-3\mu)}\right\}\frac{\mathrm{norm}_i}{V_i} \tag{B6}$$

$$= \frac{1}{\Lambda^{\mathrm{XS}}(T_i,\, Z_i;\, \Delta E)}\,\frac{3}{\left(r_i^3 - r_{i-1}^3\right)}\int_{r_{i-1}}^{r_i}\rho_g^2(r)\Lambda^{\mathrm{XS}}(T(r),\, Z(r);\, \Delta E) r^2\, dr, \tag{B7}$$

where $V_i = (4\pi/3)(r_i^3 - r_{i-1}^3)$ is the volume of the spherical shell. Note, however, that many deprojection programs like PROJCT in XSPEC and others based on the widely used "onion-peeling" deprojection method (Fabian et al. 1981) give norm_i with respect to the volume, $(4\pi/3)(r_i^2 - r_{i-1}^2)^{3/2}$, representing the intersection of the 3D shell with the cylinder of the same inner and outer radii (see eq. [B12]). In this case the integral in equation (B7) must proceed over the intersecting volume and therefore depends not only on r. Typically we perform the radial integrations by dividing up the shells into 5–10 subshells each of constant ρ_g and Λ^{XS}, where the volume of each subshell j is $\sum_{k=m(i-1)+1}^{j} V_{kj}^{\mathrm{int}}$ using the definitions associated with equations (B11) and (B12) in the projection analysis below. The quantity $(\langle\rho_g^2\rangle_i)^{1/2}$ is a measure of the average density within the relevant volume (intersecting or total) of the spherical shell.

The average temperature within the shell i is given by

$$\langle T\rangle_i = \frac{\int_{r_{i-1}}^{r_i} T(r)\rho_g^2(r)\Lambda^{\mathrm{XS}}(T(r),\, Z(r);\, \Delta E) r^2\, dr}{\int_{r_{i-1}}^{r_i}\rho_g^2(r)\Lambda^{\mathrm{XS}}(T(r),\, Z(r);\, \Delta E) r^2\, dr}, \tag{B8}$$

where, as above, the integration proceeds instead only over the intersecting volume if necessary. We set $\langle T\rangle_i = T_i$, which holds exactly for constant Λ^{XS} within the shell. (Similarly, for any abundance, such as iron, we set $\langle Z_{\mathrm{Fe}}\rangle_i = Z_{\mathrm{Fe},i}$.) Since Λ^{XS} generally varies monotonically with increasing radius within the shell, this association becomes increasingly more accurate as the shell width is allowed to decrease. However, even if calibration uncertainties and other issues associated with the detector response can be ignored, systematic errors associated with, e.g., background subtraction, assumption of spherical symmetry, and Galactic absorption may bias the inferred 1T model fitted to the multicomponent spectral data over a limited energy range. It is therefore essential to examine the sensitivity of one's analysis to such effects as we have done here and previously (Lewis et al. 2003; Buote & Lewis 2004; Humphrey et al. 2006; Zappacosta et al. 2006).

[8] In the XSPEC Users' Manual, norm_i is called K. But the term "norm" is actually displayed for this parameter for the coronal plasma models like APEC.

[9] This expression is not given in the XSPEC Users' Manual, but it follows from the definition of norm_i (i.e., K) in that manual.

Projection analysis.—This is the primary method employed in this paper. The 1T models are fitted directly to the spectra that are extracted from concentric circular annuli on the sky. Rather than dividing norm_i by the emitting volume, now we divide it by the area of the annulus, $A_i = \pi(R_i - R_{i-1})^2$, to obtain a line-of-sight, emission-weighted projection of ρ_g^2 averaged over A_i,

$$\mathrm{proj}\left\langle \rho_g^2 \right\rangle_i \equiv \left\{ \frac{4\pi[D_A(1+z)]^2}{10^{-14}} \frac{(5\mu)^2 m_u^2}{(2+\mu)(4-3\mu)} \right\} \frac{1}{A_i} \mathrm{norm}_i \tag{B9}$$

$$= \frac{1}{\Lambda^{\mathrm{XS}}(T_i, Z_i; \Delta E)} \frac{2}{\left(R_i^2 - R_{i-1}^2\right)} \int_{R_{i-1}}^{R_i} R\, dR \int_{\mathrm{LOS}} \rho_g^2(r) \Lambda^{\mathrm{XS}}(T(r), Z(r); \Delta E)\, dz, \tag{B10}$$

where $r = (R^2 + z^2)^{1/2}$ and the projection proceeds within a cylinder denoted by i defined by inner radius, R_{i-1}, outer radius, R_i, and height specified by the line-of-sight integration. (Typically we set the line-of-sight integration limits to approximately ± 1.5 virial radii, although our results are very insensitive to this choice for values greater than the virial radius.) For the special case of constant Λ^{XS} within the cylinder i we have that $\mathrm{proj}\,\langle \rho_g^2 \rangle_i$ equals $\int_{\mathrm{LOS}} \rho_g^2\, dz$ averaged over A_i (e.g., Buote & Lewis 2004).

In practice, for fast numerical evaluation it is preferable to approximate the integrations in equation (B10) in terms of the contributions from discrete shells (Kriss et al. 1983). The spherical volume of the cluster is partitioned into a series of N concentric spherical shells such that $r_0 < r_1 < r_2 < \ldots < r_N$, where the number of shells and their widths are chosen to achieve desired computational accuracy. A particular shell, $[r_{k-1}, r_k]$, is denoted by the index k of the outer radius. We define a corresponding set of N concentric circular annuli on the sky such that $R_0 = r_0 < R_1 = r_1 < \ldots < R_N = r_N$, where the origins of the annuli and shells coincide. In analogy to the 3D shells, we denote a particular annulus, $[R_{k-1}, R_k]$, by the index k of the outer radius. To ensure computational accuracy, this set of reference annuli necessarily oversamples the set of annuli used to extract the X-ray data. Consequently, for each annulus i of the data, $[R_{i-1}, R_i]$, one defines a mapping between i of the data annuli and k of the reference annuli so that the annulus i contains multiple reference annuli. It is useful to consider the case where the reference annuli oversample the data by some integer m so that $k = mi$; i.e., annulus $[R_{i-1}, R_i]$ of the data contains all reference annuli between $R_{m(i-1)}$ and R_{mi}.[10] In this case equation (B10) may be approximated as

$$\mathrm{proj}\left\langle \rho_g^2 \right\rangle_i \simeq \frac{1}{\Lambda^{\mathrm{XS}}(T_i, Z_i; \Delta E)} \frac{1}{\pi\left(R_i^2 - R_{i-1}^2\right)} \sum_{j=m(i-1)+1}^{mi} \sum_{k=j}^{N} \left(\rho_g^2 \Lambda^{\mathrm{XS}}\right)_k V_{kj}^{\mathrm{int}}. \tag{B11}$$

The inner sum $\sum_{k=j}^{N}$ projects $(\rho_g^2 \Lambda^{\mathrm{XS}})_k \equiv \rho_g^2(\bar{r}_k)\Lambda^{\mathrm{XS}}(T(\bar{r}_k), Z(\bar{r}_k); \Delta E)$ into reference annulus j, where $\bar{r}_k$ represents an intermediate radius within shell k. The projection is carried out via the matrix

$$V_{kj}^{\mathrm{int}} = \frac{4\pi}{3}\left[\left(r_k^2 - R_{j-1}^2\right)^{3/2} - \left(r_k^2 - R_j^2\right)^{3/2} + \left(r_{k-1}^2 - R_j^2\right)^{3/2} - \left(r_{k-1}^2 - R_{j-1}^2\right)^{3/2}\right], \qquad k \geq j, \tag{B12}$$

representing the volume of shell k that intersects the cylinder defined by the width of annulus j and infinite height (Kriss et al. 1983). If any terms in equation (B12) have negative arguments, they must be set to zero; e.g., if $k = j$, then $V_{kk}^{\mathrm{int}} = (4\pi/3)(r_k^2 - r_{k-1}^2)^{3/2}$, as noted above in the deprojection analysis.

The average temperature within annulus i is given by

$$\langle T \rangle_i = \frac{\int_{R_{i-1}}^{R_i} R\, dR \int_{\mathrm{LOS}} T(r)\rho_g^2(r)\Lambda^{\mathrm{XS}}(T(r), Z(r); \Delta E)\, dz}{\int_{R_{i-1}}^{R_i} R\, dR \int_{\mathrm{LOS}} \rho_g^2(r)\Lambda^{\mathrm{XS}}(T(r), Z(r); \Delta E)\, dz} \tag{B13}$$

$$\simeq \frac{\sum_{j=m(i-1)+1}^{mi} \sum_{k=j}^{N} \left(T\rho_g^2 \Lambda^{\mathrm{XS}}\right)_k V_{kj}^{\mathrm{int}}}{\sum_{j=m(i-1)+1}^{mi} \sum_{k=j}^{N} \left(\rho_g^2 \Lambda^{\mathrm{XS}}\right)_k V_{kj}^{\mathrm{int}}}, \tag{B14}$$

where again we set $\langle T \rangle_i = T_i$ with the same caveats noted above in the deprojection analysis.

Response weighting.—The existence of radial gradients in the temperature and abundances of galaxy groups and clusters implies that the X-ray spectra evaluated over spherical shells or circular annuli of finite width are not 1T coronal plasmas. In theory, fitting a 1T model to such a multicomponent plasma yields average values of the spectral parameters norm_i, T_i, and Z_i suitable for comparison with the emission-weighted spherical models described previously. Unfortunately, biased parameter values can result from such 1T fits. Fitting a 1T coronal plasma model to a multitemperature spectrum with average temperature near 1 keV and solar abundances results in a severe underestimate of the iron abundance ("Fe bias;" see Buote & Fabian 1998; Buote 2000b, 2000c). But since the inferred temperature is not biased (Buote 2000c) and the abundance underestimate does not translate to a large overestimate of the gas density, the effect on the derived mass profile is minimal. Note that the Fe bias primarily originates from the differences between the strengths of the Fe L-shell lines in single-temperature and multitemperature plasmas, not from effects related to the detector response other than restricted bandwidth.

However, since the effective area of the detector responses of ACIS on *Chandra* and EPIC on *XMM-Newton* (as well as detectors on previous X-ray satellites like *ROSAT*) peaks near 1 keV, fitting a 1T model to a spectrum having a range of temperature components above 1 keV will tend to yield a temperature that is biased low (Mazzotta et al. 2004; Vikhlinin 2006). This effect is most pronounced for

[10] Since the data do not extend out to the adopted edge of the system, it follows that $r_N \gg r_{mD}$, where D is the number of data annuli.

the "projection analysis" of galaxy clusters possessing in each annulus a wide range of temperatures above ~3 keV where the Fe L-shell lines are weak. (At lower temperatures, the Fe bias applies as noted above.) Approximate methods to account for this effect have been proposed by Mazzotta et al. (2004) and Vikhlinin (2006).

Our more rigorous approach is a straightforward averaging of the plasma emissivity over the detector response for the (projected) region in question. Let the response matrix that determines the probability a photon of energy E will be detected in PHA bin n be denoted by $\mathrm{RSP}_i(n, E)$, where i denotes the annulus on the sky as defined in the projection analysis above. This response matrix is usually considered to be the product of a "redistribution matrix," $\mathrm{RMF}_i(n, E)$, and an "auxiliary response file," $\mathrm{ARF}_i(E)$, the latter of which contains the information on the effective area. Then the count rate in PHA bin n is proportional to $\rho_g^2 \sum_E \Lambda^{\mathrm{XS}}(T, Z; E)\mathrm{RSP}_i(n, E)$, where the sum is over all energies in the response matrix. By summing over all PHA bins n corresponding to the energy range $[E_1, E_2]$, and since ρ_g^2 does not depend on the convolution, we may account for the detector response in our above presentation by replacing Λ^{XS} with

$$\overline{\left[\Lambda^{\mathrm{XS}}(T, Z; \Delta E)\right]_i} \equiv \sum_n \sum_E \Lambda^{\mathrm{XS}}(T, Z; E)\mathrm{RSP}_i(n, E), \tag{B15}$$

where we have not renormalized since the normalization of Λ^{XS} does not need to be specified for proj $\langle \rho_g^2 \rangle_i$ and $\langle T \rangle_i$.

Although applying this response weighting helps to mitigate the temperature bias for hot systems, this procedure is still not formally equivalent to that used to obtain T_i, Z_i, and norm_i by fitting a 1T model to a spectrum containing multiple temperature and abundance components. To avoid the Fe bias and response bias altogether, the projected spherical models must be fitted directly to the observed spectra. This means that, rather than predicting quantities that are integrated over the bandpass, one must predict the photon count rate $C_{i,n}$ in circular annulus i for each PHA bin n,

$$\begin{aligned} C_{i,n} &= \left\{ \frac{10^{-14}}{2[D_A(1+z)]^2} \frac{(2+\mu)(4-3\mu)}{(5\mu)^2 m_u^2} \right\} \int_{R_{i-1}}^{R_i} R\, dR \int_{\mathrm{los}} dz\, \rho_g^2(r) \sum_E \Lambda^{\mathrm{XS}}(T(r), Z(r); E)\mathrm{RSP}_i(n, E) \\ &\simeq \left\{ \frac{10^{-14}}{4\pi[D_A(1+z)]^2} \frac{(2+\mu)(4-3\mu)}{(5\mu)^2 m_u^2} \right\} \sum_{j=m(i-1)+1}^{mi} \sum_{k=j}^{N} V_{kj}^{\mathrm{int}} \left(\rho_g^2\right)_k \sum_E \left[\Lambda^{\mathrm{XS}}(E)\right]_k \mathrm{RSP}_i(n, E), \end{aligned} \tag{B16}$$

such as done, essentially, in a procedure like SMAUG (Pizzolato et al. 2003). Note that $(\rho_g^2)_k \equiv \rho_g^2(\bar{r}_k)$ and $[\Lambda^{\mathrm{XS}}(E)]_k \equiv \Lambda^{\mathrm{XS}}(T(\bar{r}_k), Z(\bar{r}_k); E)$ with $\bar{r}_k$ an intermediate radius in shell k as above.

It is our experience that even for systems possessing the highest quality data available from *Chandra* and *XMM-Newton*, the magnitudes of statistical errors and the key systematic errors noted above are sufficiently large so that presently there is little advantage to increasing the sophistication of the model comparison beyond that expressed by equation (B15). (Note also that we do not use SMAUG in this paper because its current implementation in XSPEC does not include the parametric mass fitting approach in § 6.) However, it is expected that data from the next generation of X-ray satellites (*Constellation-X*, *Xeus*) will be of sufficiently high quality to require the direct fitting approach for large numbers of systems, provided that there is strict control of other systematic errors.

REFERENCES

Akritas, M. G., & Bershady, M. A. 1996, ApJ, 470, 706
Allen, S. W., Schmidt, R. W., Ebeling, H., Fabian, A. C., & van Speybroeck, L. 2004, MNRAS, 353, 457
Allen, S. W., Schmidt, R. W., & Fabian, A. C. 2001, MNRAS, 328, L37
Arnaud, K. A. 1996, in ASP Conf. Ser. 101, Astronomical Data Analysis Software and Systems V, ed. G. H. Jacoby & J. Barnes (San Francisco: ASP), 17
Arnaud, M., Neumann, D. M., Aghanim, N., Gastaud, R., Majerowicz, S., & Hughes, J. P. 2001, A&A, 365, L80
Arnaud, M., Pointecouteau, E., & Pratt, G. W. 2005, A&A, 441, 893
Arnaud, M., et al. 2002, A&A, 390, 27
Barcons, X., Mateos, S., & Ceballos, M. T. 2000, MNRAS, 316, L13
Bartelmann, M., & Steinmetz, M. 1996, MNRAS, 283, 431
Bernardi, M., Hyde, J. B., Sheth, R. K., Miller, C. J., & Nichol, R. C. 2007, AJ, 133, 1741
Blanton, E. L., Sarazin, C. L., McNamara, B. R., & Clarke, T. E. 2004, ApJ, 612, 817
Böhringer, H., Matsushita, K., Churazov, E., Ikebe, Y., & Chen, Y. 2002, A&A, 382, 804
Borgani, S., et al. 2004, MNRAS, 348, 1078
Bridges, T., et al. 2006, MNRAS, 373, 157
Bullock, J. S., Kolatt, T. S., Sigad, Y., Somerville, R. S., Kravtsov, A. V., Klypin, A. A., Primack, J. R., & Dekel, A. 2001, MNRAS, 321, 559
Buote, D. A. 2000a, ApJ, 532, L113
———. 2000b, ApJ, 539, 172
———. 2000c, MNRAS, 311, 176
Buote, D. A., Brighenti, F., & Mathews, W. G. 2004, ApJ, 607, L91
Buote, D. A., & Fabian, A. C. 1998, MNRAS, 296, 977
Buote, D. A., Gastaldello, F., Humphrey, P. J., Zappacosta, L., Bullock, J., Brighenti, F., & Mathews, W. 2007, ApJ, 664, 123
Buote, D. A., & Lewis, A. D. 2004, ApJ, 604, 116
Buote, D. A., Lewis, A. D., Brighenti, F., & Mathews, W. G. 2003, ApJ, 594, 741
Buote, D. A., & Tsai, J. C. 1995, ApJ, 439, 29
Cavaliere, A., & Fusco-Femiano, R. 1978, A&A, 70, 677
De Grandi, S., & Molendi, S. 2002, ApJ, 567, 163
De Luca, A., & Molendi, S. 2004, A&A, 419, 837
de Vaucouleurs, G., de Vaucouleurs, A., Corwin, H. G., Jr., Buta, R. J., Paturel, G., & Fouque, P. 1991, Third Reference Catalogue of Bright Galaxies (Berlin: Springer)
Dickey, J. M., & Lockman, F. J. 1990, ARA&A, 28, 215
Dolag, K., Bartelmann, M., Perrotta, F., Baccigalupi, C., Moscardini, L., Meneghetti, M., & Tormen, G. 2004, A&A, 416, 853
El-Zant, A. A., Hoffman, Y., Primack, J., Combes, F., & Shlosman, I. 2004, ApJ, 607, L75
Evrard, A. E., Metzler, C. A., & Navarro, J. F. 1996, ApJ, 469, 494
Fabian, A. C., Hu, E. M., Cowie, L. L., & Grindlay, J. 1981, ApJ, 248, 47
Faltenbacher, A., Kravtsov, A. V., Nagai, D., & Gottlöber, S. 2005, MNRAS, 358, 139
Finoguenov, A., Davis, D. S., Zimer, M., & Mulchaey, J. S. 2006, ApJ, 646, 143
Finoguenov, A., Ponman, T. J., Osmond, J. P. F., & Zimer, M. 2007, MNRAS, 374, 737
Fisher, D., Illingworth, G., & Franx, M. 1995, ApJ, 438, 539
Freeman, P. E., Kashyap, V., Rosner, R., & Lamb, D. Q. 2002, ApJS, 138, 185
Fukazawa, Y., Kawano, N., & Kawashima, K. 2004, ApJ, 606, L109
Gastaldello, F., Ettori, S., Molendi, S., Bardelli, S., Venturi, T., & Zucca, E. 2003, A&A, 411, 21
Gavazzi, G., Pierini, D., & Boselli, A. 1996, A&A, 312, 397
Girardi, M., Borgani, S., Giuricin, G., Mardirossian, F., & Mezzetti, M. 2000, ApJ, 530, 62
Gnedin, O. Y., Kravtsov, A. V., Klypin, A. A., & Nagai, D. 2004, ApJ, 616, 16

Gustafsson, M., Fairbairn, M., & Sommer-Larsen, J. 2006, Phys. Rev. D, 74, 123522
Holmberg, J., Flynn, C., & Portinari, L. 2006, MNRAS, 367, 449
Hu, W., & Kravtsov, A. V. 2003, ApJ, 584, 702
Humphrey, P. J., & Buote, D. A. 2006, ApJ, 639, 136
Humphrey, P. J., Buote, D. A., Gastaldello, F., Zappacosta, L., Bullock, J. S., Brighenti, F., & Mathews, W. G. 2006, ApJ, 646, 899
Irwin, J. A., Athey, A. E., & Bregman, J. N. 2003, ApJ, 587, 356
Jarrett, T. H., Chester, T., Cutri, R., Schneider, S., Skrutskie, M., & Huchra, J. P. 2000, AJ, 119, 2498
Jing, Y. P. 2000, ApJ, 535, 30
Kaastra, J. S., et al. 2004, A&A, 413, 415
Khosroshahi, H. G., Jones, L. R., & Ponman, T. J. 2004, MNRAS, 349, 1240
Kochanek, C. S., et al. 2001, ApJ, 560, 566
Komatsu, E., & Seljak, U. 2001, MNRAS, 327, 1353
Koranyi, D. M., & Geller, M. J. 2002, AJ, 123, 100
Kotov, O., & Vikhlinin, A. 2005, ApJ, 633, 781
Kriss, G. A., Cioffi, D. F., & Canizares, C. R. 1983, ApJ, 272, 439
Kroupa, P. 2001, MNRAS, 322, 231
Kuhlen, M., Strigari, L. E., Zentner, A. R., Bullock, J. S., & Primack, J. R. 2005, MNRAS, 357, 387
Lewis, A. D., Buote, D. A., & Stocke, J. T. 2003, ApJ, 586, 135
Lin, Y.-T., & Mohr, J. J. 2004, ApJ, 617, 879
Loeb, A., & Peebles, P. J. E. 2003, ApJ, 589, 29
Łokas, E. L., Wojtak, R., Gottlöber, S., Mamon, G. A., & Prada, F. 2006, MNRAS, 367, 1463
Lumb, D. H., Warwick, R. S., Page, M., & De Luca, A. 2002, A&A, 389, 93
Macciò, A. V., Dutton, A. A., van den Bosch, F. C., Moore, B., Potter, D., & Stadel, J. 2007, MNRAS, 378, 55
Mahdavi, A., Finoguenov, A., Böhringer, H., Geller, M. J., & Henry, J. P. 2005, ApJ, 622, 187
Mamon, G. A., & Łokas, E. L. 2005, MNRAS, 362, 95
Mandelbaum, R., Seljak, U., Cool, R. J., Blanton, M., Hirata, C. M., & Brinkmann, J. 2006, MNRAS, 372, 758
Maraston, C. 1998, MNRAS, 300, 872
Markevitch, M., Forman, W. R., Sarazin, C. L., & Vikhlinin, A. 1998, ApJ, 503, 77
Markevitch, M., et al. 2003, ApJ, 583, 70
Mathews, W. G. 1978, ApJ, 219, 413
Mathews, W. G., Faltenbacher, A., Brighenti, F., & Buote, D. A. 2005, ApJ, 634, L137
Mathiesen, B. F., & Evrard, A. E. 2001, ApJ, 546, 100
Mazzotta, P., Rasia, E., Moscardini, L., & Tormen, G. 2004, MNRAS, 354, 10
Mohr, J. J., Mathiesen, B., & Evrard, A. E. 1999, ApJ, 517, 627
Molendi, S. 2004, in IAU Colloq. 195, Outskirts of Galaxy Clusters: Intense Life in the Suburbs, ed. A. Diaferio (Cambridge: Cambridge Univ. Press), 122
Morris, R. G., & Fabian, A. C. 2005, MNRAS, 358, 585
Mulchaey, J. S. 2000, ARA&A, 38, 289
Nagai, D., Vikhlinin, A., & Kravtsov, A. V. 2007, ApJ, 655, 98
Navarro, J. F., Frenk, C. S., & White, S. D. M. 1995, MNRAS, 275, 720
———. 1997, ApJ, 490, 493
Navarro, J. F., et al. 2004, MNRAS, 349, 1039 (N04)
Neumann, M., Reich, W., Fuerst, E., Brinkmann, W., Reich, P., Siebert, J., Wielebinski, R., & Truemper, J. 1994, A&AS, 106, 303
Nevalainen, J., Markevitch, M., & Forman, W. 2000, ApJ, 532, 694
Nevalainen, J., Markevitch, M., & Lumb, D. 2005, ApJ, 629, 172
O'Sullivan, E., Vrtilek, J. M., Kempner, J. C., David, L. P., & Houck, J. C. 2005, MNRAS, 357, 1134
O'Sullivan, E., Vrtilek, J. M., Read, A. M., David, L. P., & Ponman, T. J. 2003, MNRAS, 346, 525
Padmanabhan, N., et al. 2004, NewA, 9, 329
Pahre, M. A. 1999, ApJS, 124, 127
Parker, L. C., Hudson, M. J., Carlberg, R. G., & Hoekstra, H. 2005, ApJ, 634, 806
Piffaretti, R., Jetzer, P., Kaastra, J. S., & Tamura, T. 2005, A&A, 433, 101
Pizzolato, F., Molendi, S., Ghizzardi, S., & De Grandi, S. 2003, ApJ, 592, 62
Pointecouteau, E., Arnaud, M., & Pratt, G. W. 2005, A&A, 435, 1
Pradas, J., & Kerp, J. 2005, A&A, 443, 721
Pratt, G. W., & Arnaud, M. 2002, A&A, 394, 375
———. 2005, A&A, 429, 791
Pratt, G. W., Boehringer, H., Croston, J. H., Arnaud, M., Borgani, S., Finoguenov, A., & Temple, R. F. 2007, A&A, 461, 71
Prugniel, P., & Simien, F. 1997, A&A, 321, 111
Rasia, E., et al. 2006, MNRAS, 369, 2013
Rines, K., & Diaferio, A. 2006, AJ, 132, 1275
Russell, P. A., Ponman, T. J., & Sanderson, A. J. R. 2007, MNRAS, 378, 1217
Salpeter, E. E. 1955, ApJ, 121, 161
Sato, S., Akimoto, F., Furuzawa, A., Tawara, Y., Watanabe, M., & Kumai, Y. 2000, ApJ, 537, L73
Saxton, R. D., & Siddiqui, H. 2002, The Status of the SAS Spectral Response Generation Tasks for XMM-EPIC (XMM-SOC-PS-TN-43; Garching: ESA)
Schindler, S. 1996, A&A, 305, 756
Seigar, M. S., Graham, A. W., & Jerjen, H. 2007, MNRAS, 378, 1575
Spergel, D. N., et al. 2003, ApJS, 148, 175
———. 2007, ApJS, 170, 377
Sun, M., Forman, W., Vikhlinin, A., Hornstrup, A., Jones, C., & Murray, S. S. 2003, ApJ, 598, 250
———. 2004, ApJ, 612, 805
Tasitsiomi, A., Kravtsov, A. V., Gottlöber, S., & Klypin, A. A. 2004, ApJ, 607, 125
Thomas, P. A., Muanwong, O., Pearce, F. R., Couchman, H. M. P., Edge, A. C., Jenkins, A., & Onuora, L. 2001, MNRAS, 324, 450
Vikhlinin, A. 2006, ApJ, 640, 710
Vikhlinin, A., Kravtsov, A., Forman, W., Jones, C., Markevitch, M., Murray, S. S., & Van Speybroeck, L. 2006, ApJ, 640, 691
Vikhlinin, A., Markevitch, M., Murray, S. S., Jones, C., Forman, W., & Van Speybroeck, L. 2005, ApJ, 628, 655
Wechsler, R. H., Bullock, J. S., Primack, J. R., Kravtsov, A. V., & Dekel, A. 2002, ApJ, 568, 52
Xue, Y.-J., Böhringer, H., & Matsushita, K. 2004, A&A, 420, 833
Zappacosta, L., Buote, D. A., Gastaldello, F., Humphrey, P. J., Bullock, J., Brighenti, F., & Mathews, W. 2006, ApJ, 650, 777